Accepted to J. Renew. Sustain. Energy 10.1063/5.0161905

Case study of a bore wind-ramp event from lidar measurements and HRRR simulations over ARM Southern Great Plains

Yelena L. Pichugina[1, 2], Robert M. Banta[1, 2], E.J. Strobach[1, 2], B.J. Carroll[1, 2], W. Alan Brewer[2], D.D. Turner[3], V. Wulfmeyer[4], E. James[3], T.R. Lee[5], S. Baidar[1,2], J.B. Olson[3], R.K. Newsom[6], H.-S. Bauer[4], and R. Rai[6]

[1]CIRES, University of Colorado, Boulder, CO 80309, USA
[2]NOAAChemical Sciences Laboratory, Boulder, CO 80305, USA
[3]NOAA Global Systems Laboratory, Boulder, CO 80305 USA
[4]University of Hohenheim, Institute of Physics and Meteorology, Stuttgart, 70599, Germany
[5]NOAA Air Resources Laboratory, Oak Ridge, TN 37830, USA
[6]Pacific Northwest National Laboratory, Richland, WA 99352, USA

Correspondence to: Yelena Pichugina (Yelena.Pichugina@noaa.gov)

Abstract

The rapid change of wind speed and direction on 21 August 2017 is studied using Doppler lidar measurements at 5 sites of the Atmospheric Radiation Measurement (ARM) Southern Great Plains (SGP) facility in north-central Oklahoma. The Doppler lidar data were investigated along with meteorological variables such as temperature, humidity, and turbulence available from the large suite of instrumentation deployed at the SGP Central Facility (C1) during the Land-Atmosphere Feedback Experiment (LAFE) in August 2017. Lidar measurements at 5 sites, separated by 55 – 70 km, allowed us to document the development and evolution of the wind flow over the SGP area, examine synoptic conditions to understand the mechanism that leads to the ramp event and estimate the ability of the High-Resolution Rapid Refresh (HRRRv3) model to reproduce this event. The flow feature in question is an atmospheric bore, a small-scale phenomenon that is challenging to represent in models, that was generated by a thunderstorm outflow northwest of the ARM SGP area. The small-scale nature of bores, its impact on power generation, and the modeling challenges associated with representing bores are discussed in this paper. The results also provide information about model errors between sites of different surface and vegetation types.

Accepted to J. Renew. Sustain. Energy 10.1063/5.0161905

1. Introduction

In wind energy, rapid changes in wind speed over a short period of time ranging from a few minutes up to several hours are defined as wind "ramp events". These wind ramps may lead to significant fluctuations in the power generated by wind turbines. In practice, an increase in wind speed or wind power has been defined as a "ramp-up", and a decrease, as a "ramp-down" event (Lee et al. 2012, Worsnop et al. 2018). Fluctuations of wind-turbine power on sub-hourly, hourly, or daily time scales may affect the overall power generated by the wind plant and may bring large uncertainties to power scheduling and trading (Ela and Kemper, 2009).

Wind-power ramps have been broadly defined as significant changes in production over a relatively short time, but various definitions of power ramps are provided in the literature, depending on the magnitude and duration of the event, where magnitude is considered with respect to the rated power (P_{rated}) of the wind farm. The limits on key quantities that define ramps – the change in wind power production (ΔP) and the period (Δt) of this change vary among studies. For example, Gallego et al. (2014) defined power ramps as having Δt ranging from 30 min to 3 hours and ΔP within 20 -75% of the turbine-rated power; Greaves et al. (2009) defined power ramps with ΔP about 50% of the installed wind capacity that occurs within less than 4 hours; Bossavy et al. (2010) define a power ramp as when a ΔP of ~ 50% occurs over one hour. In addition to the magnitude ΔP and duration Δt, power ramps have been characterized in the literature by the ramp rate ΔP/ Δt, the starting or central time of the event, the type of the ramp (ramp-up or ramp-down), and the ramp gradient (Sherry and Rival, 2015; Ferreira et al. 2010). Other ramp features, such as ramp shape, diurnal cycle, and seasonality, are discussed in several case studies (Pichault et al., 2020).

Power ramps associated with a significant increase or decrease of wind speed (wind ramps) can be driven by different atmospheric conditions (Freedman et al. 2008). *At local scales*, processes driven by horizontal gradients of surface heating, such as sea breezes (Wharton et al. 2011), sea-breeze-generated marine intrusions (Banta et al. 2020), and cold-pools (Pichugina et al. 2019; Wilczak et al. 2019; McCaffrey et al. 2019; Adler et al. 2023) can cause wind ramps. The atmospheric flow phenomena known as low-level jets (LLJs), can also amplify wind speed (Freedman et al. 2008). LLJs have been studied for their meteorological importance and frequency, especially in the Great Plains where they are present on about 20% to 65% of days depending on the season and year (Bonner 1968; Mitchell et al. 1995; Whiteman et al. 1997; Song et al. 2005; Carroll et al. 2019). Along with the direct importance for wind energy through strong wind speed and shear, LLJs can indirectly impact productivity by promoting convection through moisture transport and low-level convergence (Geerts et al. 2015; Berg et al 2015). Basic information on LLJs is provided in Appendix B. More information on LLJ properties and nighttime evolution analyzed from Doppler lidar measurements as well as the variability between ARM SGP sites can be found in Pichugina et al. (2023).

The presence of LLJs and the post-sunrise growth of the planetary boundary layer have been identified as dominant factors of ramp events in Deppe et al. (2012). Shorter-duration power ramps are mainly influenced by mesoscale systems, whereas synoptic systems tend to be responsible for longer-duration wind and power ramps (Drew et al. 2018). At larger scales, features such as frontal passages, density currents, and thunderstorm outflows (Freedman and Zack, 2012; DeMarco and Basu, 2018) can lead to significant changes in the wind flows.

Accurate model prediction of ramp events is necessary to anticipate and mitigate negative effects on wind-energy resource management. The improvement of models used in the wind-energy industry, from frequent updates of model physics, parameterization schemes, and horizontal grid spacing, requires evaluation of model skills through comparisons with observations (Olson et al. 2019, Shaw et al. 2019, Wilczak et al. 2019, Banta et al. 2023). Dedicated field campaigns have been conducted to address this challenge. The High-Resolution Rapid Refresh (HRRR) numerical weather prediction model was continuously updated during the second Wind Forecast Improvement Project (WFIP2, Olson et al. 2019) and all improvements from version 1 (HRRRv1) to version 4 (HRRRv4) were evaluated against various types of remote sensors (lidars, sodars, and wind-profiling radars) and in-situ measurements (Banta et al. 2020, 2021, 2023; Bianco et al. 2019; Draxl et al. 2021, Olson et al. 2019, Pichugina et al. 2019, 2020, 2022; Rai et al. 2020, Wilczak et al. 2019). Different methods of probabilistic ramp forecasts from the HRRR were compared to measurements from two tall towers located in western Colorado and eastern Oregon of the United States (Worsnop et al 2018), and valuable information was obtained on the uncertainty and improved model skill over the raw forecasts.

Measurements from remote-sensing instruments distributed over an area may provide insight into wind and power ramps over wind-farms. For example, during WFIP2, fluctuations of wind-speed from scanning Doppler lidar measurements at three sites along the Columbia River Valley approximated the fluctuations of total power generated within the Bonneville Power Authority (BPA) balancing area (Pichugina et al. 2020, Wilczak et al. 2019). The largest power ramps (up to 3 GW or more) were found for westerly gap-flows in summer and cold pools in winter months (McCaffrey et al. 2019, Pichugina et al. 2019, 2020).

During the Land-Atmosphere Feedback Experiment (LAFE), conducted at the Central Facility (C1) of the Atmospheric Radiation Measurement (ARM) Southern Great Plains (SGP) atmospheric observatory in August 2017 (Wulfmeyer et al. 2018), fluctuations of nocturnal wind speed were measured by Doppler lidar on several nights. The north-central Oklahoma location of this observatory is known for its nocturnal maximum in thunderstorm activity and precipitation (Wallace 1975; Fritsch et al. 1986; Tripoli and Cotton 1989), and most of the significant wind-ramping fluctuations observed were associated with flow features ultimately caused by thunderstorms. The largest (~12 m s^{-1}) ramp-down was a transient disturbance observed on 21 August 2017 (Fig. 1), starting just before 1100 UTC (UTC = local time + 6h) at site C1. Measurements from scanning Doppler lidars were also available at four SGP extended facilities. Datasets from the network of lidars provide an exceptional opportunity to estimate the spatial variability of this significant ramp event over the SGP area, to identify weather-related causes of the sudden change of wind speed, and to quantify the ability of the HRRR NWP-model simulations to capture the ramp event as observed at the five ARM SGP sites on this day.

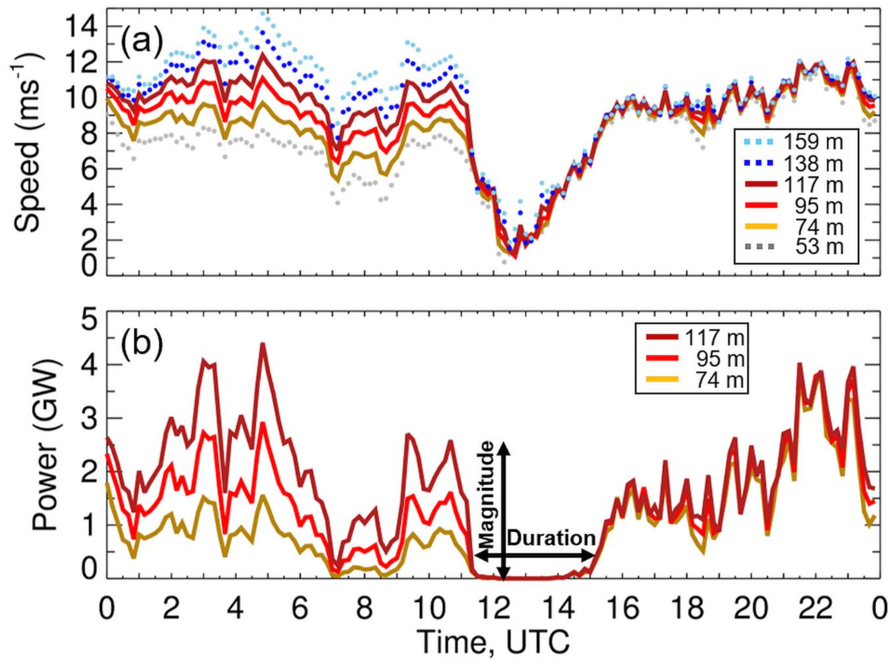

Figure 1. (a) Time-series of wind speed at 6 heights from lidar measurements at SGP site C1. (b) Wind power calculated for the "virtual" turbine with the rotor diameter of 70 m and wind speed from (a) taken at three heights (74 m, 95 m, and 117 m). Black arrows indicate the magnitude and duration of the power ramp event for the wind turbine with the hub-height of 117 m.

The paper is organized as follows. Section 2 provides the location of Doppler lidar sites, a description of available measurements and temporal and vertical resolutions of obtained profiles. A brief overview of the HRRR version 3 (HRRRv3) used in this study is also provided in this section. Section 3 discusses a larger-scale context of the synoptic situation during the ramp-down event on 21 August. Section 4 presents the results of the ramp events from Doppler and Raman lidar measurements at the central facility. Section 5 shows the spatial variability of the wind speed ramp from lidar and measurements at 5 SGP sites, illustrates the influence of the wind ramp on the power production of a hypothetical wind turbine, and provides analysis of winds and AERI-measured temperature fields. Section 6 estimates the ability of 3-km HRRRv3 hourly simulations to capture the vertical structure and temporal evolution of the wind ramp event.

Temperature and humidity from NOAA/NCRP's North American Regional Reanalysis (NARR) and wind speed from the Experimental High Resolution Rapid Refresh (HRRRX) model are provided in Appendix A to support the possible cause of the observed ramp event.

2. Description of SGP lidar sites and measurements.

Scanning Doppler lidars were located at the ARM SGP central facility (C1) and the four extended facilities E32, E37, E39, and E41 separated by 56-57 km along the south-north and 66-77 km along the east-west directions (Fig. 2). The sites have different surface and vegetation types from cropland to grassland and pasture, and site elevations vary between 279 and 379 m ASL (Pichugina et al. 2023, Table 1). Sites C1 and E41 are surrounded by wind farms. The closest wind turbine to the lidar at C1 is located to the south at 3.74 km and from the lidar at E41 to the southwest at 2.52 km. The terrain and trees in some areas add more complexity to measured winds and the uncertainty of lidar data from low-elevation scans. Quality control of the line-of-sight velocities (Newsom and Krishnamurty, 2020), allowed the removal of outliers and provided accurate profile data.

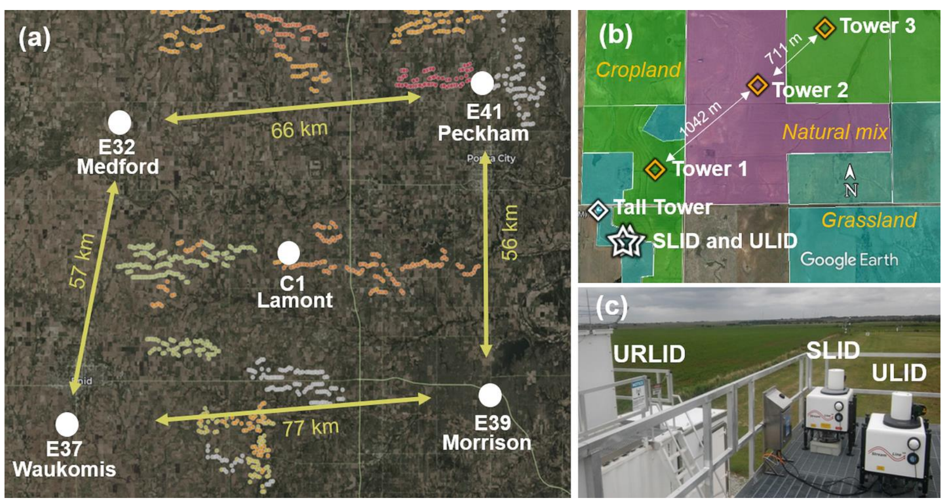

Figure 2 (a) Map of the ARM SGP Doppler lidar sites (white circles) and the surrounding wind farms (small circles). The colors indicate wind turbines of different capacities and owners (https://eerscmap.usgs.gov). Yellow lines show distances between sites. (b) Location of 10-m towers, 60-m tall tower and lidars (SLID, DLID and Raman lidar at C1. (c) Detailed view of lidar locations at C1.

The lidars at all five sites are Halo Photonics Stream Line scanning systems that continuously operated in synchronized scanning modes providing multi-year datasets of wind speed, wind direction, and three components of the wind vector. Profiles of all these variables from 91 m up to several km above ground level (AGL), obtained at a temporal resolution of 10-min and a vertical resolution of ~26 m are available at the ARM SGP archive https://www.arm.gov/capabilities/observatories/sgp. Details of the deployment history, raw and processed data description, along with other valuable information and sample plots, can be found in Newsom and Krishnamurty (2020).

2.1. Instrumentation deployed for LAFE

In August 2017, additional measurement systems, including various types of lidar, were deployed to the central facility (LAFE; Wulfmeyer et al. 2018). The German University of Hohenheim (UHOH) deployed a scanning Doppler lidar (ULID) that operated at C1 from 13 Aug to 6 Sep 2017 in a six-beam VAD scanning mode to obtain profiles of wind speed and direction having a temporal resolution of 1 min and turbulence profiles at a temporal resolution of 5 min. Turbulence profiles include TKE, vertical fluxes of horizontal momentum, and variances of wind vector components, computed from a 6-beam measurement technique (Sathe et al. 2015; Bonin et al. 2017). The vertical resolution of all variables is ~21 m. In addition, the UHOH Raman Doppler lidar (URLID, Hammann et al. 2015; Behrendt et al. 2015) provided temperature and humidity profiles at 10-min temporal and 30-m resolutions from 30 m up to several km AGL. During the LAFE, the ARM SGP lidar (SLID) at C1 operated in staring mode providing only vertical-velocity data. All three lidars (ULID, SLID, and URLID) were deployed side-by-side (Wulfmeyer et al. 2018).

Various data, including wind and temperature, were also available at C1 from sonic anemometers installed at 25 m and 60 m on the 80-m meteorological tower located ~ 250 m from SLID. Standard meteorology, surface fluxes, soil temperature, moisture, and radiation were also available at 2.5 and 10 m from three NOAA / ARL surface energy balance towers (Lee and Buban, 2020; Lee et al. 2021) located along a southwest-northeast transect at distances of ~ 0.7-1 km over cropland (Towers 1 and 3) and the natural-vegetation mix (Tower 2).

2.2. HRRRv3: The model used in the study

The NOAA-developed numerical weather prediction (NWP) model (Benjamin et al. 2016) used in this study is an updated third version of the 3-km HRRR (High Resolution Rapid Refresh) model, i.e., HRRRv3. The HRRRv3 domain encompasses the continental United States, providing wind forecasts every hour (Table 1). The HRRRv3 was in the transition-to-operations stage during 2016-2018 and became operational in October 2018 (James et al. 2022). Table 1 provides the physics configuration of the HRRRv3 model, adapted from Dowell et al. 2022. The previous version of the HRRR, the HRRRv2, operational during Oct 2016-Oct 2018 (James et al, 2022), is used in some examples to illustrate the difference between HRRR versions. The full description of the HRRRv3 along with other HRRR versions (HRRRv1-HRRRv3), modifications, and improvements can be found in Dowell et al. (2022), and the improvements in performance for specific forecast problems are documented for all HRRR versions in James et al. (2022) along with a comprehensive list of previously published articles evaluating specific aspects of HRRRv3 performance.

Table. 1 Physics configuration for HRRRv3.

Model	WRF-ARWv3.8.1+
Domain	CONUS, Alaska
Init Frequency	1h, 3h
Map	Lambert conformal projection stereographic (AK)
Grid points (x,y)	1800 x 1060; 1300 x 920
Grid spacing	3 km
Vertical layers	51
Pressure top	20 hPa
Lateral boundary conditions	RAP
Initial conditions	RAP post-DFI plus; 1-h spinup, 3-km GSI with GDAS
Vertical coordinate	Hybrid sigma - terrain-following
Horizontal/ Vertical advection	Fifth-order upwind
Scalar advection	Positive definite advection
Large time step	20 s
Upper -level damping	Rayleigh, dampcoef = 0.2 s-1, zdamp =5000 m
Computational horizontal diffusion	6th order (0.25), horizontal only (not on slopes), applied to all variables
Run frequency	Hourly
Forecast duration	36h every 6h, otherwise 18h
Radiation	RRTMG

Land surface, including number of layers	RUC LSM, 9 soil levels, 2-layer snow (v3.8+)
Land use	30” MODIS
Planetary boundary and surface layer	Mellor-Yamada- Nakanishi-Niino (v3.8+)
Subgrid-scale clouds	MYNN prognostic SGS cloud fraction, cloud water
Orographic drag	small-scale orographic drag
Cloud Microphysics	Thompson- Eidhammer “aerosol aware” (v3.8)
Microphysics temperature tendency limit	0.07 K s^{-1}

For verification of HRRRv3 against lidar measurements, the gridded model output was extracted at the position of the lidar by bilinear interpolation from the surrounding four grid points. Using other extraction techniques, such as cubical interpolation or taking output from the nearest grid point, show similar results with correlation coefficients of 0.99 between the extraction techniques, differences in mean wind speed of 0.01 to 0.22 m s^{-1}, and standard deviations < 0.085 m s^{-1} (Pichugina et al. 2020). Modeled values obtained at the location of each lidar were then linearly interpolated to the heights of lidar measurement. The effects of the vertical-interpolation method and uncertainties of two approaches—first, when measurements are interpolated to model output levels (lidar-to-model), and second, when modeled variables are interpolated to the heights of lidar measurements (model-to-lidar)—are discussed and the second approach (model-to-lidar) is adopted, as justified in Pichugina et al. (2017).

For quantitative comparisons of modeled and measured wind-speed profiles, lidar measurements were hourly averaged to match the time interval of model output.

3. Larger-scale context

3.1 Great Plains nocturnal thunderstorms, gust fronts, and bores

Thunderstorms generate cold outflows and density currents (gust fronts). When these outflows push through a surface-based stable layer, such as a nocturnal inversion, they can create a wave ahead of the gust front in the form of a bore or a solitary wave, as shown by Knupp (2006). Bores are a form of gravity wave in the lower atmosphere, representing a superposition or “packet” of gravity wavelengths. They form in and propagate through a layer of positive static stability (i.e., where potential temperature θ increases with height z, or $d\theta/dz > 0$), and nighttime temperature inversions often provide good conditions for bore propagation. The speed of propagation of the waves increases with stronger atmospheric stability. NWP modeling studies suggest that the speed may also depend on the depth of the stable layer ahead of and behind the bore (e.g., Osborne and Lapworth 2017), and that other conditions, such as the alignment or misalignment of forcing associated with the large-scale synoptic and the mesoscale phenomenon that generates bores, can modify convergence and bore propagation. Moreover, the influence of diabatic heating is a relatively unexplored topic that additionally adds to the complexity of gust front/bore evolution.

Bores form when the stable flow encounters an obstacle, which can be moving. The bore develops ahead (upwind) of the obstacle. Over the U.S. Great Plains, as described, this obstacle is often a thunderstorm gust front, an organized mesoscale cold front or density current, formed when a cool downdraft spreads out laterally in the form of surface divergence as it hits the surface. Environmental stable-layer wind speeds on the order of 15-20 m s^{-1}, and speed profiles exhibiting LLJ structure—a maximum in the lowest several hundred meters—have been known to support the bore formation (e.g., Haghi et al. 2017, 2019). Climatologically over the Great Plains, these conditions are routinely met in the warm season during the frequent occurrences of nocturnal southerly LLJs, for example, Song et al. (2005) found that southerly LLJs occur in 63 % of warm-season nights in this region. Thus, when thunderstorms initiate in that region, gust fronts and bores are a regular occurrence, and have been documented in several previous studies (e.g., Koch et al. 1991, 2008a,b; Knupp 2006; Loveless et al. 2019, Toms et al. 2017; Mueller et al. 2017; Haghi et al. 2017, 2019; Parsons et al. 2019). Nocturnal Great-Plains thunderstorms are themselves a high-frequency occurrence, for example, Geerts et al. (2017) showed that over a six-year summertime period, convective precipitation was observed more than twice per week on average over much of the Great Plains.

In surface-tower measurements, bores are most identifiable as an abrupt increase in surface pressure and a windshift toward its direction of propagation. Effects on temperature and humidity near the surface are often minor. Knupp (2006, his Fig.7) shows a pressure bump of ~3 hPa accompanied by a drop in wind speed very similar to that depicted here in Fig.1, the wind also veering in time. A major difference between solitary waves (solitons), another common disturbance, and bores is that solitary waves are vertical oscillations where recovery back to pre-disturbance conditions is rapid, whereas the effects of a bore persist for some hours. Koch et al. (2008b) observe that in practice, by analyzing field measurement data, "it can be difficult to distinguish bores from density currents and solitons," a notion reinforced by Geerts et al. (2017, p.778) and Haghi et al. (2017, p.3933). For the present study, making such a distinction is not necessary, but for simplicity and due to the observed slow recovery of the wind speed back to pre-disturbance levels, we refer to our ramp-down as a *bore* in this study. Haghi et al. (2017) found that the frequency of bore activity increased through the night, such that the peak in bore activity was before dawn. Bores tend to move at a faster speed ahead of the gust front that formed them, and often the gust front dissipates, leaving only the bore. Bores can diminish in time as a result of environmental changes, for example if the stability increases above the layer that the bore is propagating through, wave energy can be dissipated upwards, or if the stability of the layer itself changes to become less favorable for bore propagation, either condition can result in the bore weakening.

In reflectivity data from weather radar scans, weak lines of enhanced backscatter, referred to as "fine lines," sometimes expand outwards from storm centers (an example will be shown later). Several studies have given examples of radar fine lines, associating them with storm outflow phenomena, including bores (e.g., Knupp 2006; Koch et al. 2008b; Haghi et al. 2017, 2019; Mueller et al. 2017; Toms et al. 2017). Thus storm radars can be used to detect fine lines, which is often helpful in short-term forecasting of these kinds of flow disturbances. Many studies have associated bores with nocturnal mesoscale convective systems over the U.S. Great Plains (Blake et al. 2017; Haghi et al. 2019; Knupp 2006; Koch et al. 2008a; Koch et al. 2008b; Parsons et al. 2019). Additionally, bores have been observed over numerous locations worldwide, including Australia (Davies et al., 2017), the UK (Osborne and Lapworth, 2017), Mexico (Martin and Johnson, 2008), and China (Zhang et al. 2020). More details on the formation of internal bores in the atmosphere (Rottman and Simpson 1989) can be found in recent studies (Haghi et al. 2017; Parsons et al. 2019) along with the diagram of flow regimes for two-layer flow over a streamlined obstacle.

Recent research contributions to the understanding of bores and other outflow phenomena have come from the 2002 International H2O Project (IHOP) and the 2015 Plains Elevated Convection At Night (PECAN) project. Both of these studies were primarily aimed at understanding the initiation and propagation of warm-season rainfall and severe-weather events in the Great Plains, important to agriculture and public safety there. Parsons et al. (2017) used IHOP data to study the role of outflow mechanisms in generating new convection, and Stelten and Gallus (2017), and Parker (2021) used case studies from the PECAN dataset for their numerical modeling studies. The generation of new storm activity leads to new storm outflow phenomena, which alter the winds in the rotor layer of wind turbines.

From a WE forecasting perspective, it is important to understand that NWP models show poor skill in simulating, and thus predicting, the initiation and movement of moist convection, which includes cumulus clouds that grow into thunderstorms. If the storm initiation is off, then outflow features generated by the storms will be even more poorly modeled, and secondary storm initiation from those outflows, as well as the outflows from *those* secondary storms, even worse than that. Storm outflows include gust fronts, which significantly increase wind speeds and thus up-ramps in wind-power generation, whereas bores often produce large drops in wind speed, as in the present example, and thus also large drops in wind energy generated. Improving the ability of NWP forecast models to predict storm initiation and development is an important ongoing objective of atmospheric research today.

To address these important modeling research goals, these datasets were also used for NWP case studies. In general, the models were able to produce the initiation and movement of storms and the outflows they generated (Stelten and Gallus 2017; Blake et al. 2017; Johnson et al. 2018; Parker 2021). Quantitatively, however, the location, timing, and intensity of the storms and outflows have led to significant errors (Gao et al. 2017; Feng et al. 2018). For example, in results from initial, "pristine" storms that were reasonably well simulated, Stelten and Gallus (2017) noted that mean timing errors were 1-1.7 h and location errors, 77-105 km in the first initiation of Plains convection by five models. Commenting on this study, Parker (2021) notes that these models were, "not particularly skillful in terms of the initial timing and location of mesoscale convective system development," a general sentiment expressed in many of the articles mentioned. We note that one forecast model, the Rapid Refresh (RAP), in which the HRRR is nested, addresses this after a storm shows up on the operational radar analysis by adjusting the model's dynamic and thermodynamic fields to account for the existence of the storm (Benjamin et al. 2016). Thus, although the model may miss the initiation of the storms, their effects are represented in forecasts for model runs initialized after the storms appear on operational radars. Overall, the accurate prediction of nocturnal convective systems as well as bores commonly generated by convective outflows (Haghi et al. 2017) in the warm season over the Great Plains remains a challenge for numerical weather prediction models (Zhang et. al, 2019).

In summary, for WE the interest here is in the role of these storms in producing flows that disrupt the normal warm-season wind pattern below 200 m AGL, which on most nights in the Great Plains is dominated by the southerly LLJ. The bulk of the activity for these outflow phenomena is aloft, but they are often associated with large changes in wind speed near the surface, including the wind-turbine rotor layer. Gust fronts can produce significant ramps-up in wind speed, and bores, ramps-down as here. Probably the most important message is that features such as these have their ultimate origins in deep, moist convection (thunderstorms), and predicting convective initiation and subsequent development into rain- or thunderstorms is a difficult forecast for current-generation NWP models.

3.2 Case Study: Large-scale environment

The surface chart for 0900 UTC (Fig. 3) prior to the ramp event in Fig. 1 shows a large-scale ridge off the East Coast of the U.S., extending westward to produce southerly wind flow over the southern Great Plains, including the study region in Oklahoma. The 500-hPa chart (Fig.3b) indicates that this southerly flow occupied a deep layer over the region. Such a large-scale subtropical ridge (the "Bermuda high") extending westward from the Atlantic Ocean is typical for August, but Pichugina et al. (2023) have shown that August 2017, the month of LAFE, saw an unusually large number of frontal passages and resulting postfrontal northeasterly wind conditions compared with climatology, including a day-long rain event on 11 August. Here a stationary front stretches west to east at the surface to the north of the study area, separating the southerly flow to the south from cooler air over the northern states. A mesoscale trough passed north to south through the Oklahoma-Texas panhandles, associated with a line of thunderstorms.

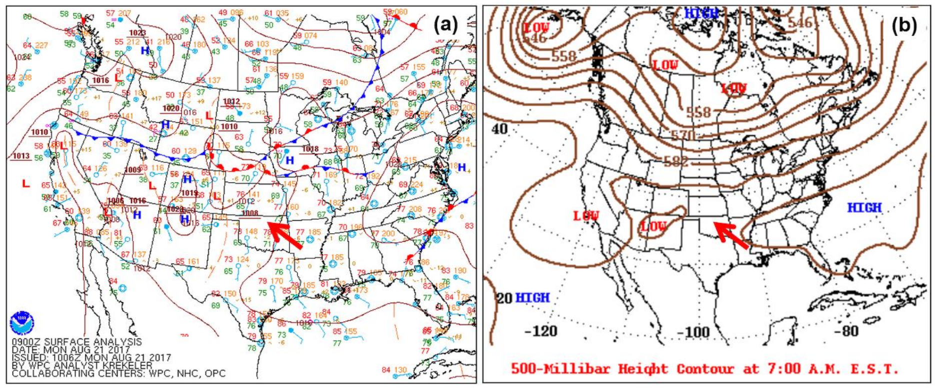

Figure 3. (a) Surface analysis chart for 0900 UTC (https://www.wpc.ncep.noaa.gov/), and (b) 500 hPa chart for 1200 UTC, 21 August 2017. Red arrows show location of SGP study sites.

Composite radar reflectivity images for 0955-1055 UTC (Fig.4) show the most likely source of the major ramp-down in Fig.1. A thunderstorm cell passed north of the study area from west to east, and radar fine lines seen in the images (red arrows) indicate storm gust-front outflow features approaching the study area from the northwest. As described in general in Section 3.1, this fine line is associated with the disturbance seen in Fig.1.

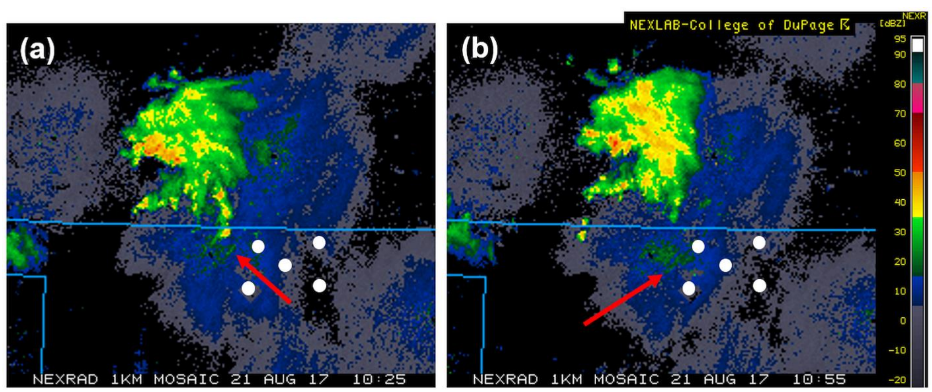

Figure 4. Composite reflectivity from NEXRAD (Next Generation Radar) 1km MOSAIC on 21 Aug 2017 at (a) 1025 and (b) 1055 UTC (https://www2.mmm.ucar.edu/imagearchive/). White dots denote approximate locations of SGP measurement sites. Red arrows emphasize radar fine lines that moved towards and through the sites from the northwest, originating from the convective system.

On the study night, the development of the LLJ from 02 to 11 UTC at Site C1 (Fig. 5a) appeared typical of southerly LLJ nights as described by Pichugina et al. (2023), until the ramp event at 1100 UTC; a minor disturbance is also noted starting at ~07 UTC. Doppler-lidar wind speed profiles (Fig. 5c) prior to 1100 UTC show the LLJ maximum speed occurring at 400 m AGL, but the depth of the turbulent stable boundary layer (SBL) was less than 200 m, by the Pichugina and Banta (2010) classification, according to which the kink in the profile at that height identifies these as Type 3 profiles (Appendix B). Potential-temperature profiles $\theta(z)$ indicate stable stratification up to 700 m. Profiles after the ramp-down in Fig. 5c, starting with 1100 UTC, indicate large wind-speed reductions up to at least 300 m; then post-sunrise convective mixing is evident in $\theta(z)$ after 1300 UTC. August sunrises in central Oklahoma are at ~1200 UTC.

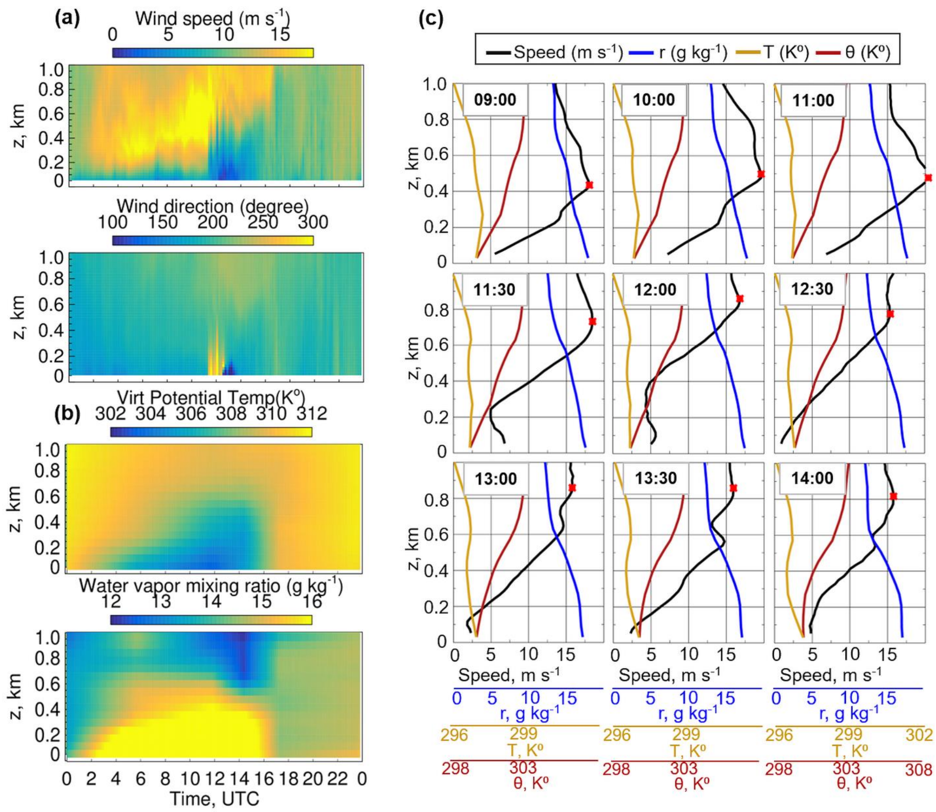

Figure 5. Diurnal variability of (a) wind speed and direction from ULID, (b) virtual potential temperature, and water vapor mixing ratio from URLID measurements in the first 1 km AGL on 21 Aug 2017 at C1. (c) 5-min profiles of data from both lidars: (black) wind speed, (blue) water vapor mixing ratio (r), (dark yellow) temperature (T), and (dark red) potential temperature (θ) are shown for selected times before (0900-1100 UTC), during (1130-1230 UTC), and after (1300-1400 UTC) the observed ramp event. Red asterisks indicate wind speed maxima (LLJ) in the wind speed profiles.

Before the ramp, the speed and direction of the LLJ peak developed in a similar manner at the five sites (Fig. 6), but the height of the LLJ maximum was more variable in time and from site to site, as found by Pichugina et al. (2023). The nighttime (0300-1000 UTC) evolution of LLJ parameters (Fig. 6a) shows a gradual increase of wind speed maxima (U_{LLJ}) at all sites, slightly stronger at the western (E32, E37) sites by the beginning of the ramp event (just after 1000 UTC at E32; after 1100 UTC at other sites). The heights of the LLJ (Z_{LLJ}) were mostly below 400 m except E32 where LLJs were higher after the weaker-disturbance event at 0500 UTC. Wind direction (Z_{LLJ}) at the windspeed maximum gradually changed from southerly to south-southwesterly through the night. Significant wind fluctuations (wind ramp) accompanied by fluctuations in wind direction, temperature, and pressure (Fig. 5a) can be considered as an undular bore. An undular bore is a wave or waves in the atmosphere that can be seen on radar or lidar images. These waves can travel across the area of wind farms causing fluctuations in wind power production. Selected profiles within 3 hours before the ramp event (Fig. 6b) illustrate the difference between LLJs for all sites and small ~30° veering of wind direction with height over the first 1 km AGL. These aspects of LLJ development are typical of a Great Plains summertime southerly LLJ (Pichugina et al. 2023).

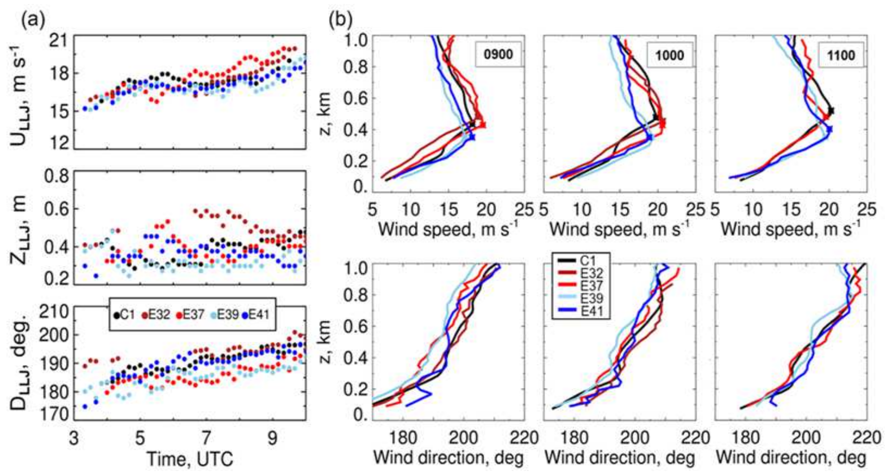

Figure 6. (a) Nighttime (0300-1000 UTC) evolution of LLJ parameters at five sites on 21 Aug 2017: U_{LLJ} - the strongest wind speed in each 10-min wind speed profile below 1 km AGL (or jet nose), Z_{LLJ} - the height of the jet nose, and D_{LLJ} - the wind direction at the jet nose. Colors indicate LLJ parameters for each site according to the legend in the bottom panel. (b) Profiles of wind speed and direction for selected times (0900, 1000, and 1100 UTC) before the ramp-down of wind speed which started around 1030 UTC at E32, 1120 UTC at C1, and around 1200 UTC at the other 3 sites. Symbols on the top panels indicate LLJ nose (U_{LLJ}). Profiles of wind speed and direction at E32 were omitted for 1100 UTC since the ramp event started earlier at this site.

At the extended sites, other aspects of LLJ development were less typical of southerly-jet nights (Fig. 7). A significant dip in wind speed arrived at the northwestern Site E32 at 0500 UTC. The storms seen in the radar images in Fig. 4 were due west of the study site at 05-06 UTC (Fig. 22 Appendix C), and most likely generated this disturbance. The winds gradually recovered

Accepted to J. Renew. Sustain. Energy 10.1063/5.0161905

through 0800-0900 UTC, just before the major ramp-down event at 1000 UTC. This lesser disturbance, which will be discussed again later, faded as it progressed, as a weaker, shorter-lived lull arrived at the southwesterly Site E37 an hour later, and even weaker disturbances were seen at the other sites after 0700 UTC. At C1 this drop in wind speed was noted at 07 UTC (Fig.5a).

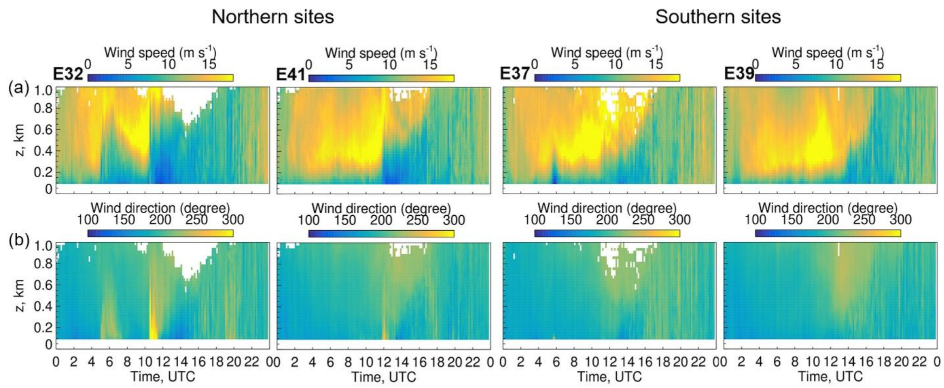

Figure 7. Spatial variability of wind flows between SGP sites: (a) wind speed, (b) wind direction from SLID 10-min measurements on 21 Aug 2017. The larger ramp event was observed at the northern sites E32 and E41 compared to the southern sites E37 and E39. The white areas on each panel indicates missing data. The color scale for (a) wind speed is shown up to 20 m s^{-1} to reveal the LLJs occurrence before the wind ramp-down event.

4. Observed wind ramp during LAFE

4. 1 Time-series of wind flow at C1

The August 2017 LAFE study period exhibited a variety of low-level wind flow patterns associated with LLJs, including many nights having northeasterly jets, as described. Lidar measurements (Fig. 8) show significant day-to-day variability of wind speed and wind direction as well as diurnal variability, with stronger nighttime wind magnitudes and larger shear in the first 1 km AGL compared to daytime (Pichugina et al. 2023). Modest wind-speed fluctuations that would lead to WE power variation were mostly less than 3 m s^{-1}, during the evening transition and at other times on most nights. For example, Fig.8 shows these kinds of routine variations on nights having strong (0-15 m s^{-1}) southerly and moderate (4-12 m s^{-1}) south-easterly winds (20-25 August) and on a weaker-wind night (30 August). The variations of wind speed during these days and over the study period were relatively small in magnitude and much shorter in time compared

Accepted to J. Renew. Sustain. Energy 10.1063/5.0161905

to the major ramp event observed on 21 August. Thus, these fluctuations would unlikely present a serious risk to wind-farm operations, because wind power (P) was still being generated (P>0), although at a reduced, hard-to-predict level.

On 21 August much larger wind-speed fluctuations were observed at C1 at all heights across a typical wind-turbine "rotor layer" of 53-138 m and higher, up to 200 m (Fig. 8, 21 Aug). Several periods of small ramping (~2-3 m s^{-1}) and relatively constant shear are seen before the larger ramp-down (> 15 m s^{-1}) event that started around 11 UTC and lasted about 5 hours, including the daytime recovery back to 10 m s^{-1} southerly flow. Wind directions before this event were mostly from the south, then veered ~120 degrees through a deep layer during the event, as in the bore studied by Knupp (2006).

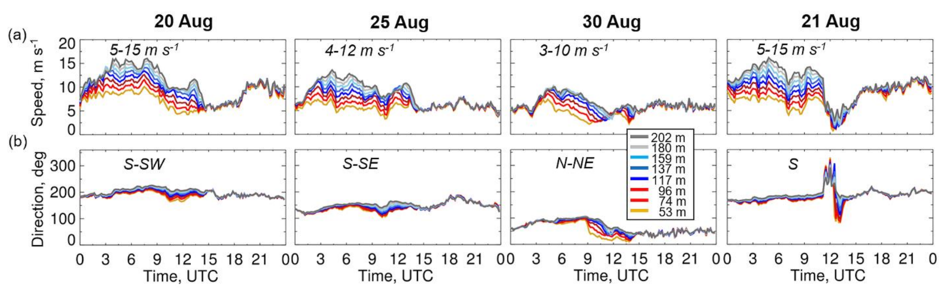

Figure 8. Time series of (a) wind speed and (b) wind direction from ULID measurements at C1 are shown for selected days (20, 25, and 30 Aug), and for 21 Aug 2017 when a large ramp event was observed. Winds are shown at several heights through the 53-202 m layer and indicated by colors according to the color table. Range of wind speed and prevailing wind directions at each panel is provided for 0-15 UTC.

Wind-speed and wind-direction ramps at C1 on this day were also observed by in-situ measurements averaged over 30-min intervals. At 1100 UTC sonic anemometer measurements at 25 and 60 m AGL on the 80-m meteorological tower (Fig. 9b) indicate the ~5-hour ramp-down-and-recovery event with 5 m s^{-1} and 7 m s^{-1} decreases in wind speed. Even lower, cup-anemometers at 2.5 and 10 m AGL from three flux stations located near but not at C1 (Fig. 9a) indicate two small ramp-down events of wind speed (~ 3 m s^{-1}) and wind direction at ~0700 and 1300 UTC. After 1000 UTC a rise in surface pressure of more than 2 hPa (Fig.9c) marked the beginning of the major drop in wind speed of the bore-generated, ramp-down episode, an effect also noted in other bore case studies (e.g., Knupp 2006; Koch et al. 2008; Toms et al. 2017; Blake et al. 2017). Sudden veering of the wind (to westerly or northwesterly) and small fluctuations (flux stations) or drops (80-m tower) in temperature are also consistent with the previous bore examples. The smaller event evident at E32 at 05 UTC can be seen as a drop in speed in the 80-m tower measurements here at ~07 UTC, and a drop in speed and a wind shift at the flux-tower sites. Although the drop in wind speed and the shift to westerly (the direction toward the storm cells) resemble bore behavior, any pressure rises associated with his feature were small at these sites, making the nature of this disturbance unclear. After sunrise the wind speed increased steadily along with the daytime increases of temperature.

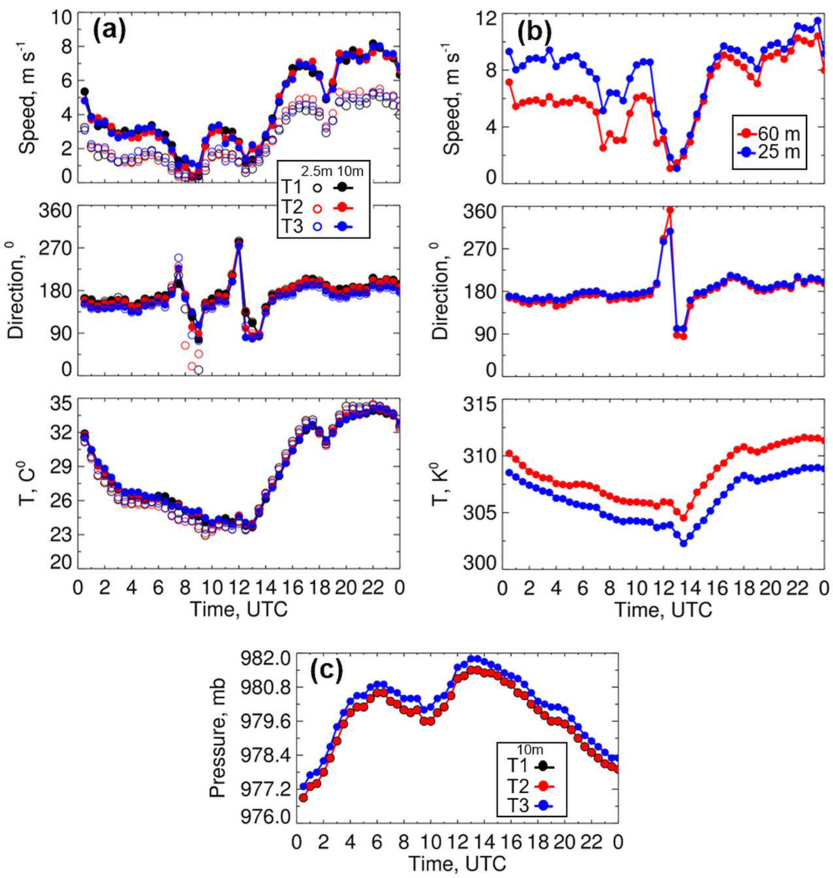

Figure 9. Time-series of a wind speed, direction, and temperature on 21 Aug from (a) cup anemometer measurements from energy balance flux stations (T1-T3) at (open circles) 2.5 m and (filled circles) 10 m; (b) 30-min sonic anemometer measurements at 25 m and 60 m on an 80-m meteorological tower. (c) Barometric pressure at 10 m at the flux stations in (a).

4.2. Vertical structure of the wind flow

Time-height cross sections and profiles of wind speed, direction, temperature, and humidity have been presented in Fig. 5. The combined effects of data availability from ULID and URLID at C1 allow us to investigate the diurnal variability of key variables in the first 1 km AGL and examine the changes in profiles of these variables before, during, and after the ramp event (Fig. 5c). As noted, development of the LLJ prior to the event was typical of a southerly-LLJ night, a deep LLJ forming a peak of 20 m s^{-1} at 400 m and a stable θ profile up to 700 m.

During the event (Fig. 5c, 1100-1200 UTC profiles), the drop in wind speed at C1 was especially dramatic between 200 and 300 m AGL, and the wind shifted to a west-northwesterly direction, more directly aligning with the direction of propagation of the bore. The spatial variability of the ramp-down among the four extended sites (Fig. 7) appears as a more significant reduction of wind speed and a larger wind-direction veer at northern sites (E32 and E41) compared to the southern sites (E37 and E39). Differences in the magnitude and timing of the wind-speed ramp event are evident among sites (Fig. 7a), but some similarities can be noted such as the occurrence of the LLJs before the ramp-down in the lowest several hundred meters. The wind direction (Fig. 7b) below 400 m at all sites, that had been south-southeasterly (150°) before the ramp, changed to south-westerly and westerly during the ramp for a short period at the northern sites. The departure of the bore and the restoration of stronger southerly flow after 1300 UTC occurred in conjunction with the onset of daytime heating and vertical mixing after sunrise, the effects of which can be seen in the wind and θ profiles in Fig. 5c.

The relative humidity and potential temperature retrieved from the Atmospheric Emitted Radiance Interferometer (AERI) at the five sites (Fig. 10a-b) indicate a moistening and a 5-6 C° cooling across a layer near the surface several hundred meters deep during the ramp event. The moistening and cooling are more evident over E32 and C1 compared to the others sites, and coincide with a stronger reduction in the near-surface potential temperature gradient structure as shown in Figure 10c. These changes reflect the proximity of these sites to the storm and the propagation direction of the outflow-generated bore northwest of the ARM site (recall Figure 4), and illustrate the impact of a passing bore on the stability structure as well as the disruption of a strongly sheared flow (Figures 5 and 7). The relatively larger decrease in stability at E32 and C1 that coincides with deeper moist layers extending a kilometer or so deep in Figure 10a suggests stronger turbulence production associated with the passage of the bore. The rapid vertical displacement and overturning that destabilizes the low-level atmospheric structure resembles to the results of Blake et. al. (2017), particularly the moistening near the surface. Furthermore, the larger reduction in the potential temperature gradient within the 100 m to 400 m layer indicates a stronger response near the surface, which would affect more of the rotor layer.

Accepted to J. Renew. Sustain. Energy 10.1063/5.0161905

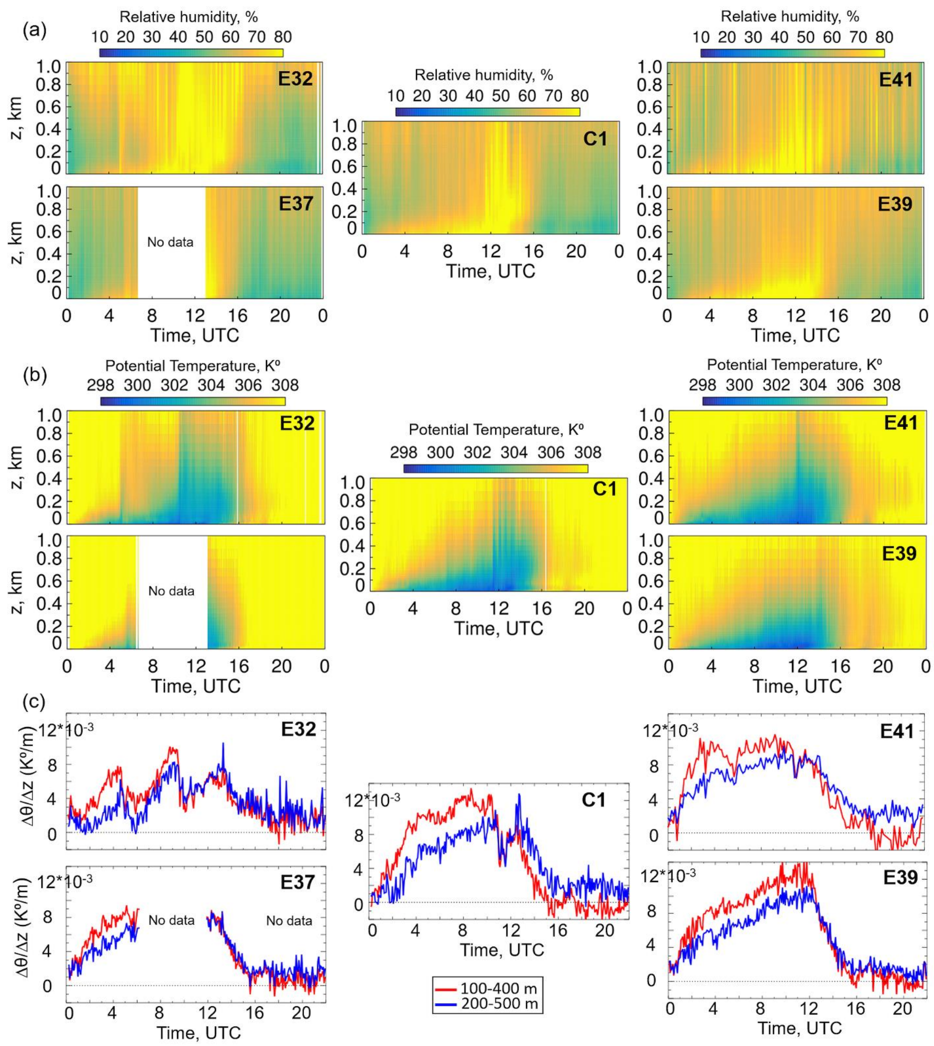

Fig. 10. Time-height cross sections of (a) Potential Temperature (θ) and (b) Relative Humidity (RH) retrievals from AERI (Atmospheric Emitted Radiance Interferometer) at 5 sites. (c) Time-series of the Potential Temperature shear (Δθ/Δz) through the layer (red) 100-400 m and (blue) 200-500 m) from AERI retrievals. Data (Turner and Loehnert, 2014) for each site are shown according to the site location (Fig. 2).

5. Spatial variability of winds during observed ramp event

Comparing measurements from lidars at the five SGP sites (Fig. 2) reveals wind-flow variations due to distances between instruments resulting in measuring atmospheric variables under different wind flow regimes and surface properties. During LAFE (Pichugina et al. 2023) differences in LLJ wind-speed measurements in general were evident between west (E32, E37) and east (E39, E39) sites as well as between south (E37, E39) and north (E32, E41) sites depending on the wind direction. Here the major differences are due to the propagation of the bore through the measurement array.

5. 1 Time series at 5 sites

Time-series (Fig. 11) of wind speed and wind direction from lidar measurements at several selected heights from ~100 to 700 m AGL illustrate differences among the five sites as well as shear between heights at each site.

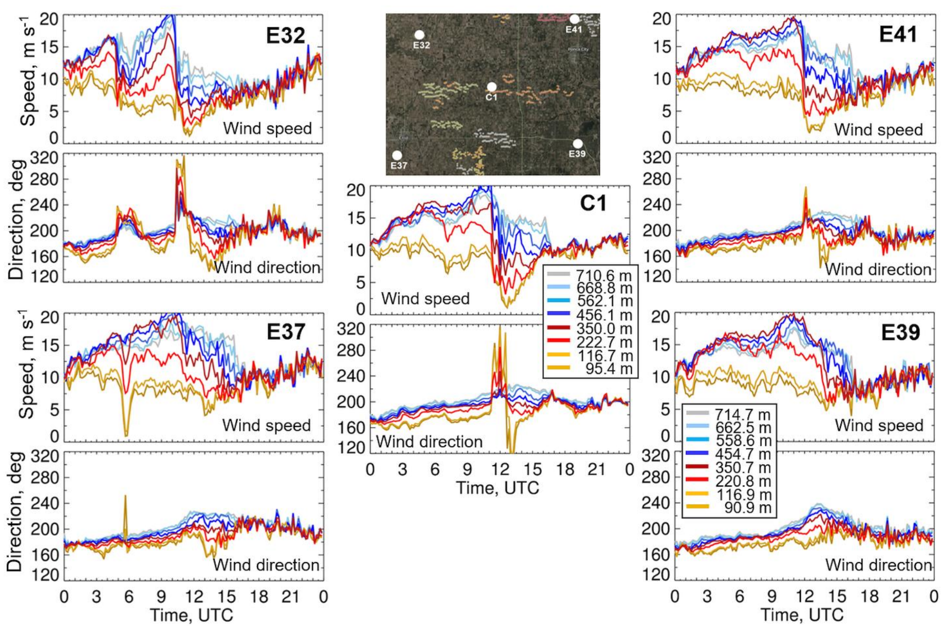

Figure 11. Time-series of wind speed and wind direction from a network of scanning Doppler lidars at the 5 ARM SGP sites on 21 August 2017. Colored lines indicate the closest available heights between ULID

Accepted to J. Renew. Sustain. Energy 10.1063/5.0161905

measurements at C1 and SLIDs measurements at the 4 extended facilities (E32-E41) according to the legends. ULID data (2Hz) is averaged over 10 min to fit the time resolution of SLIDs. Panels for each site are presented in Fig. 11 according to the site location as shown on the embedded USGS map at the top of the figure.

At C1 the largest reduction of wind speed (11.3 m s^{-1}) within the ramp-down period (1000-1300 UTC) was observed at 456 m AGL. The wind direction at the two lowest heights (95 and 117 m) significantly veered during 1100-1200 UTC changing from southerly (180º and 184º) to north-westerly (317º and 312º); then, within the next 30 min, it shifted to 128º and 178º (Tab. 2). The strongest wind shear was observed in the LLJ period before the ramp event, reaching 0.061 s^{-1} between 96 and 117 m at 0500 UTC and 0.05 s^{-1} between 222 m and 95 m at 0545 UTC. Overall, the shear observed between all heights before and during the event was strong, comparable to previous studies that found values up to 0.1 s^{-1} observed from lidar measurements in Kansas (Banta et al. 2003) and southeastern Colorado.

Significant wind ramps at the northern sites (E32 and E41) and C1 compared to the southern sites (E37 and E39) is demonstrated across different heights in Figure 12. Following the approximate propagation direction of the bore, the ramp event is first observed at E32, an hour later at C1, and 30 minutes later at E41 relative to C1. The stronger ramp event at E32 was preceded by large pre-ramp wind shear and an additional smaller wind ramp around 05 UTC. The largest down-ramp of wind speed (14.7 m s^{-1}) was observed at 456 m at E32, which was closest to the storms that produced outflows that led to the bore (recall Figure 4). The wind speed at E32 dropped from 20.7 m s^{-1} at 1000 UTC to 5.9 m s^{-1} at 1145 UTC. The wind direction at several heights changed from southerly (184-198°) at 1000 UTC to north-westerly (308-284°) at 1030 UTC, then backing to south-westerly (207-227°) at 1100 UTC. The bore diminished in amplitude as it propagated to the southeast, along with smaller reductions in wind speed and the wind-direction veer. The decreased impact from the bore to the southeast agrees with the discussion on moist-stability characteristics shown in Figure 10.

At the southern sites (E37, E39) wind speeds declined more gradually from 1100 to 1500 UTC with a slight increase in directional shear during this period. At E37 the short (~20 min), smaller down ramp previously discussed was observed around 0530 UTC at the two lowest levels with a 5.3 m s^{-1} change in wind speed and wind direction veer from 170° to 253°.

A clearer view of the propagation of the ramp through the measurement array can be obtained by plotting the time series at a given height for all sites, as shown in Fig. 12.

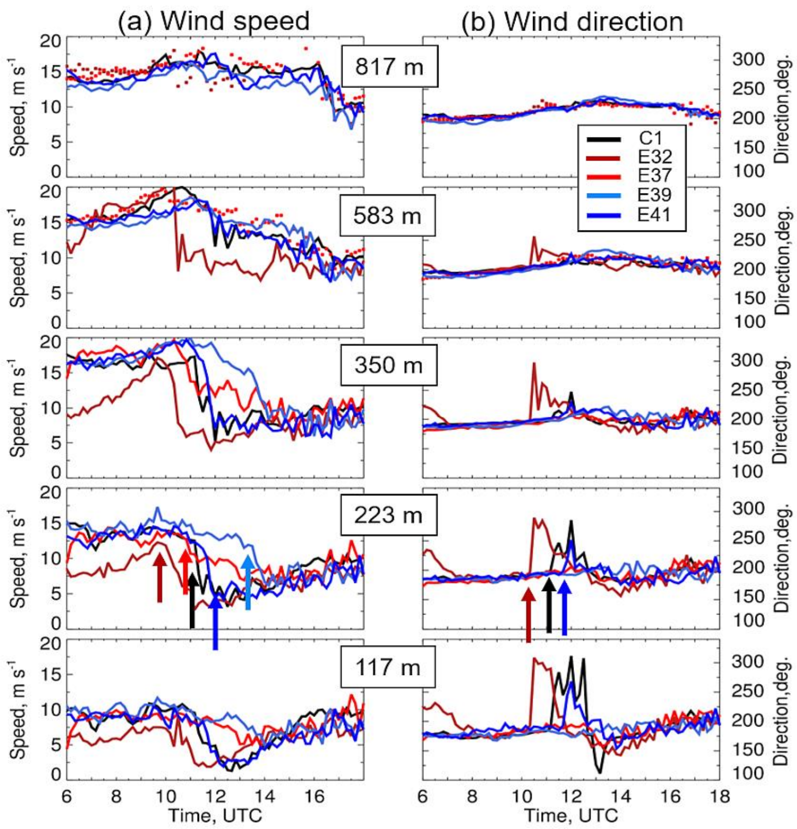

Figure 12. Time series of (a) wind speed and (b) wind direction at several heights from lidar measurements at the five sites are shown by colors according to the legend at the top right panels. Arrows at the panels for 223 m illustrate the beginning of the wind speed drop and veer of the wind direction at this particular height.

The largest response in wind speed appears in the 300-500-m AGL layer, diminishing with height until little evidence of a disturbance can be seen at 817 and 922 m AGL. The magnitude and timing of the wind ramp varied from height to height and between sites. The timing difference between sites at the beginning of the wind ramp is illustrated by the arrows on the panels for 223 m. The initial drop in wind speed and shift to west-northwesterly flow is seen at 1000 UTC at the northwest site E32, then in diminished form at the southwest site E37. The significant drop in speed and shift to westerly noted previously at C1 occurred at 1100 UTC, followed by the northeasterly site E41. Finally, the ramp passed through the southeastern site E39 starting at 1330 UTC, but as with E37, little veering of the wind occurred.

In some studies (Ahn and Hurl, 2022; Gallego et al. 2014) ramp events have been characterized by the following parameters: ramp start and end times, duration, ramp speed minimum, and the magnitude of the change in wind speed, which is the difference between the maximum and minimum of wind speed (Δsp) or wind direction veer (Δdir) during the ramp-down event. Two of these parameters (Δsp and Δdir) are shown in Fig. 13 for several heights at each site. The largest magnitude of wind-speed ramp-down (Fig. 13a) was observed at E32 (14.7 m s^{-1} at 455 m) followed by the drop at E41 (12.6 m s^{-1} at 350 m) and at C1 (11.3 m s^{-1} at 455 m). The largest wind direction veer was observed at C1 (200°) and E32 (160°) at 90 m (Fig. 13b).

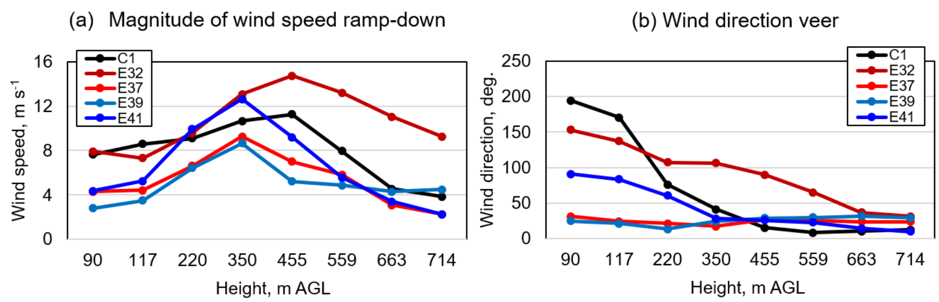

Fig. 13. Magnitude of (a) wind speed ramp-down and (b) wind direction veer at 8 heights through the layer of 90-714 m from 10-min lidar measurements at the five ARM SGP sites.

5.2 Estimate of wind-power loss due to the observed wind ramp

Strong increases or decreases in wind speed over a few hours lead to a corresponding ramping in wind power production. The impact of wind ramps on wind power-plant output has been studied in recent decades (Dalton et al. 2012, Galego et al. 2014; Lee et al. 2012; Pichault et al. 2021; Smith and Ancell, 2017; Wharton et al. 2008; Yang et al. 2013; Zhang et al. 2014). A high correlation was found between the power computed from measurements by three scanning lidars located in complex terrain, separated from each other by 30-40 km, and the total power generated over the BPA area during episodes of marine intrusions when the winds were consistently westerly (Pichugina et al. 2020). The influence that wind ramps can have on power output can be estimated for a "hypothetical" wind turbine with ~90 m hub height and 70-m rotor

Accepted to J. Renew. Sustain. Energy 10.1063/5.0161905

diameter (Fig. 14). Wind power calculated as $P = \frac{1}{2} * \rho\pi R^2 S^3\ Cp_j$, where ρ is the air density, R=35 m is the blade length or the radius of the area swept by the turbine, S is measured hub-height wind speed, and Cp_j are coefficients set to represent the power curve with 4 m s^{-1}, 25 m s^{-1}, and 12 m s^{-1} cut-in, cut-out, and rated wind speed respectively (GE Energy, 2009). The cut-in and cut-out thresholds may vary between power curves of different turbines but in common represent wind speed at which the turbine starts generating electricity or wind speed at which turbine can start spinning so fast and can be damaged. Wind speeds ranging between these two extreme points (rated winds) are favorable for turbine operations.

Fig. 14 shows that during the ramp event on 21 August, no power will be generated at the northern sites (E32, E41) and the central facility (C1) for 1h 30 min. At the southern sites (E37, E39) winds do not decrease below 4 m s^{-1} during this period and some power will still be generated. The smaller ramp event was also observed at E37 around 0530 UTC or local midnight (0030 CDT - Central Daylight Time), and the decrease of wind speed below the cut-in threshold would have led to zero power for about 30 min (0530-0600 UTC) for turbines near that site.

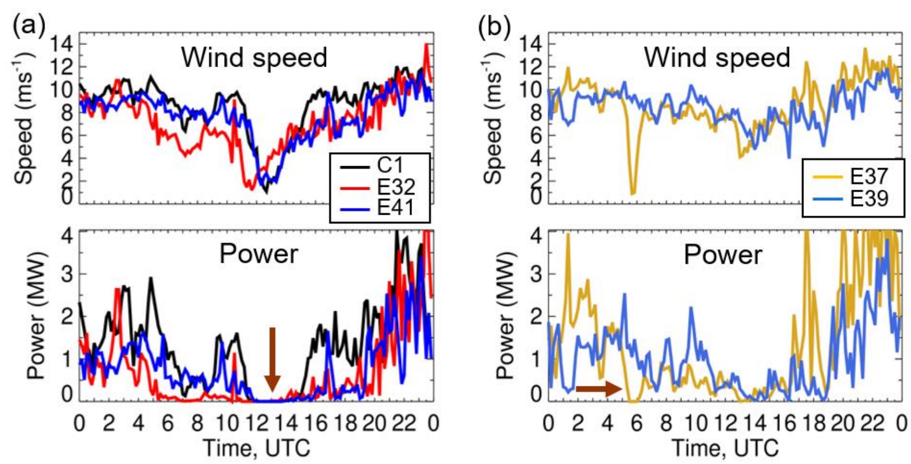

Figure 14. Time-series of wind speed from lidar measurement and computed power for a “hypothetical” wind turbine with 70 m rotor diameter are shown for (a) central (C1) and northern (E32, E41) sites, and (b) southern (E37, E39) sites. Wind speed is shown for the lowest height (91 m) of lidar measurements at E32-E41 and the closest height (95 m) from ULID at C1. (Time UTC=CDT+5h). Brown arrows point to periods of zero power.

Similar to the wind speed, a positive change in generated electrical *power* over short time intervals is defined as a "ramp-up", whereas a negative change is referred to as a "ramp down" (Ahn and Hurl, 2022; Gallego et al. 2014). The ramp parameters for wind speed and the computed power are shown in Table 2 for all five sites. The last column shows these parameters for the smaller ramp event observed at E37 around 0500 UTC.

Table 2. Ramp parameters from lidar-measured 90-m wind speed at 5 SGP sites and the period when computed wind Power (MW) equals 0.

Ramp parameters	**C1**	**E32**	**E37**	**E39**	**E41**	**E37**
Overall event time (UTC)						
Start	1030	1030	1240	1300	1100	*0500*
End	1600	1500	1400	1500	1600	*0630*
Duration	0530	0430	*0240*	*0200*	0500	*0130*
Ramp down time (UTC)						
Start	1030	1030	1240	1300	1100	*0500*
End	1240	1130	1310	1400	1240	*0545*
Duration	0210	0100	0030	0100	0140	*0045*
Ramp up time (UTC)						
Start	1240	1130	*1310*	*1400*	1240	*0545*
End	1600	1500	*1400*	*1500*	1600	*0630*
Duration	0320	0330	0110	0100	0320	*0045*
Power=0						
Start	1130	1130	1300	1400	1140	*0530*
End	1500	1330	1350	1420	1430	*0550*
Duration	**0330**	**0200**	**0050**	**0020**	**0250**	***0020***

6. HRRR evaluation: Forecast of the wind ramp

Forecasting of ramp events that occur over short temporal and spatial scales can be a difficult task, and accurate simulations of the synoptic processes leading to these dynamic changes of wind speed require models having sufficient temporal and spatial resolution (Koch et al. 2008a,b; Yang et al. 2013). In this paper, prediction of the observed wind ramp event of 21 August by NWP models was also explored. Simulations of wind flows over the ARM SGP area on that day were available from the operational HRRRv2 and the experimental HRRRv3 (which become operational in July 2018). An essential feature of the HRRR system is its rapid (hourly) updating, useful for assimilating the latest weather data. With 3-km grid spacing, the hourly-updated HRRR model provides the opportunity to better represent convection and its associated hazards. It is widely used for severe-weather, renewable-energy generation, and flash-flood forecasting (Dowell et al., 2022; James et al. 2022). Given the many difficulties in simulating storm initiation, HRRR's hourly update cycle makes it especially advantageous in overcoming many of the problems NWP models have in general in predicting nocturnal convection and the accompanying/ mesoscale phenomena. Both model versions provide forecasts with a relatively fine temporal (hourly) and spatial (3-km grid horizontal grid) resolution. Detailed descriptions of physics and parameterization schemes for all HRRR versions can be found in Dowell et al. (2022) and James et al. (2022).

In this study, HRRRv3 was evaluated against Doppler lidar measurements at five SGP sites to address how well the model simulates the spatial and vertical variability of the wind profiles, to quantify the ability of the hourly HRRRv3 outputs to capture wind ramps, to estimate model skill for several forecast lead times, and to evaluate the forecast performance for different BL conditions such as "ramp-day" versus "no-ramp day".

Fig. 15 gives a time-height cross-section overview of ULID-measured and modeled wind-speed forecasts for the 06-18 UTC time interval surrounding the ramp event, showing how model skill changed with increasing forecast lead time. The selection of initial times for both days is based on the availability of the archived HRRRv3 model outputs (00z on 21 Aug is missing) and the maximum day-ahead forecast lead time (Table 1). For comparison, the last column (Fig. 15c) shows wind speed forecasts on 21 Aug from the operational HRRRv2 model.

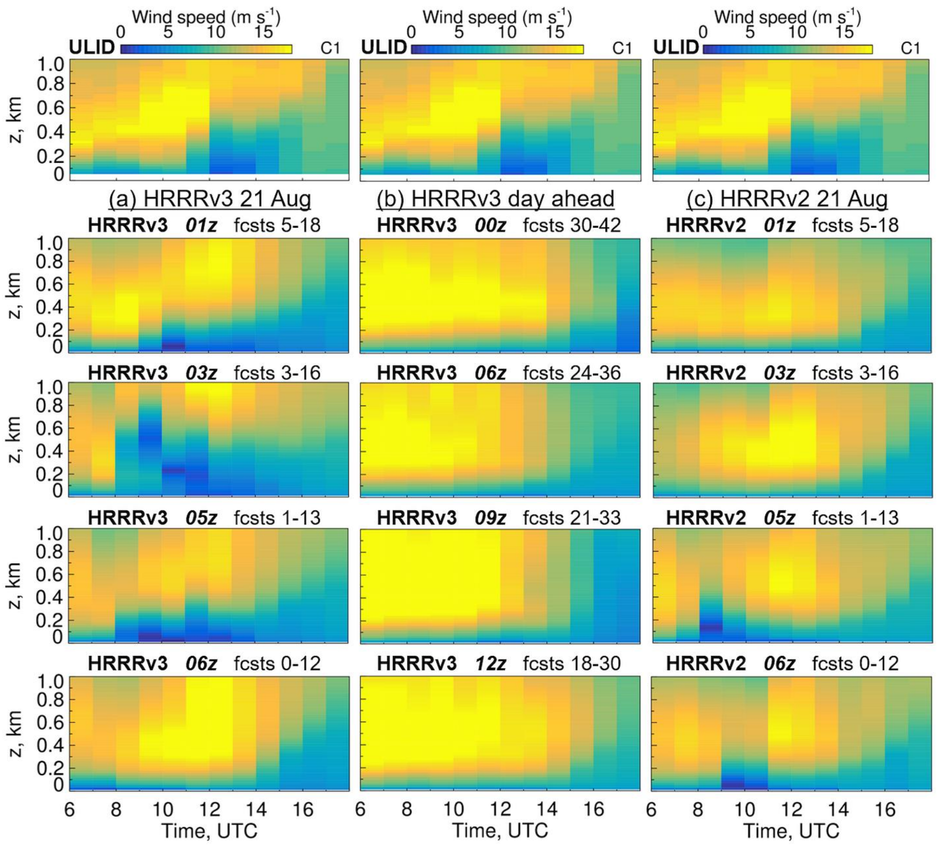

Figure 15. Wind speed from (topmost panels) hourly averaged ULID measurements at C1 and (lower panels) model forecasts valid for 0600-1800 UTC on 21 Aug. (a) HRRRv3 forecasts on 21 Aug for initial times 01z (fcsts 5-18), 03z (fcsts 3-16), 05z (fcsts 1-13), and 06z (fcsts 0-12). (b) HRRRv3 day-ahead forecasts on 20 Aug for initial times 00z (fcsts 30-42), 06z (fcsts 24-36), 09z (fcsts 21-33), and 12z (fcsts 18-30) valid for 21 Aug. (c) Same as (a) but from the operational HRRRv2 model.

All runs show a well-developed LLJ by 0600 UTC. The 00-12-h lead-time forecasts initialized at 0600 UTC (Fig. 15a) do not indicate a ramp-down disturbance, but forecasts initialized 1-, 3-, and 5-h earlier did show drops in wind speed below 300 m within the time interval displayed, although the timing was earlier than observed. Significant reductions of wind speed on 21 Aug are seen in HRRRv3 forecasts initialized at 01z and 05z, but beginning 2-3 hours earlier than measured. Forecasts initialized at 03z show reduced winds (1-3 m s^{-1}) above 400 m which are not indicated by measurements. Comparing HRRRv3 forecasts initialized at 03z on 20 Aug (day-ahead, Fig. 15b) and 21 Aug (same-day), the day-ahead runs (Fig. 15b) initialized from 20 Aug valid for 0600-1800 UTC on 21 Aug show strong winds above ~200 m with developed LLJ up to 1200 UTC but no disturbances below 200 m. Overall, no indication of the ramp event was found from all lead times (every 3 hours from 00z) for day-ahead forecasts. The operational HRRRv2 (Fig. 15c) shows some wind drop for the 05z- and 06z -times runs at 0800 UTC and 0900 UTC respectively, but shows no wind-ramp indication from other initial times such as 01z and 03z.

As pointed out in Bossavy et al. (2010), forecasts using large-temporal-scale information about ramps may lead to a significant time delay "resulting in turn to the so-called phase error". But they proposed that using ensembles to generate confidence intervals may produce better forecasts of ramp timing with more reliable confidence intervals for each look ahead time.

Time series (0600-1800 UTC) of wind speed at three lidar-measurement heights and HRRRv3 forecasts for three initial times (Fig. 16a) on 21 August demonstrate better agreement at southern sites (E37, E39), compared to the northern sites (E32, E41) and the central facility (C1) where the ramp event was most evident. Wind-speed reduction at northern sites was captured by 01z and 05z forecasts but the significant time and vertical offsets led to large errors. It is clear that significant fluctuations occurred at the northern and central sites, and the NOAA experimental HRRR (HRRRx) simulated radar reflectivity maps (Fig. 20b, Appendix A) show that a thunderstorm cell is represented in the simulation, and is the likely source of these wind disturbances. Significant timing errors in the wind ramps are noted.

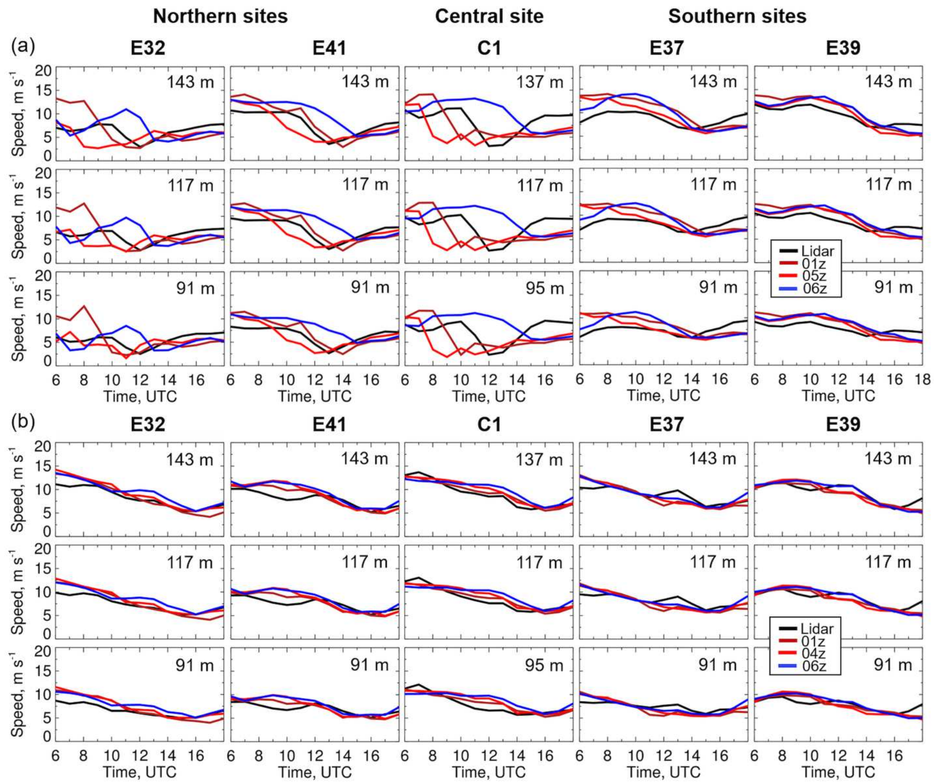

Figure 16. (a) Time-series of wind speeds on 21 Aug are shown for Northern sites (E32, E41), Central facility (C1), and Southern sites (E37, E39). Lidar data (black lines) are shown for 3 heights that are slightly different for ULID at C1 and SLIDs at E32-E41 as indicated on each panel. HRRRv3 outputs from (dark red) 01z, (red) 05z, and (blue) 06z are linearly interpolated to lidar heights at each site and shown for the forecasts valid for 0600-1800 UTC. (b). Same as Fig. 16a but for 20 Aug. Red lines show forecasts for initial time 04z because 05z is missing.

For comparison, time series of wind speed at 3 heights are shown for 20 Aug (Fig. 16b), to illustrate a better agreement between lidar measurements and HRRRv3 simulations at all five sites on a day without any significant wind fluctuations. Figure 16 shows that time offsets of the wind down-ramps between lidar and model produce larger errors at C1, followed by errors at the northern sites E32 and E41. Large errors at E37 at 0600 UTC can be explained by the offset in the forecast of the short ramp observed by lidar at this site during 0520-0610 UTC (Table 3, last column).

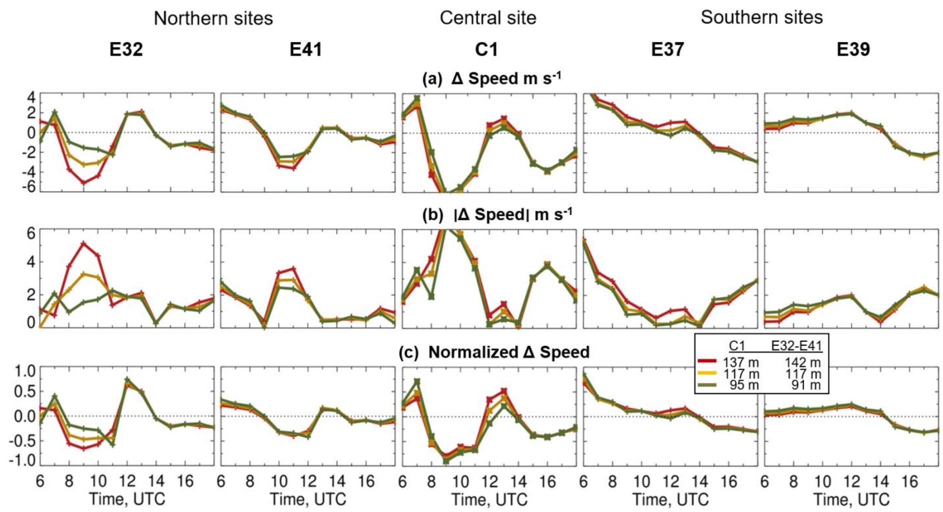

Figure 17. Time-series of wind speed (a) difference (Δ, m s^{-1}) between lidar measurements and HRRRv3 05z forecast at 5 sites on 21 Aug 2017. (b) Absolute difference (Δ, m s^{-1}), and (c) Δ speed normalized by the wind speed from lidar. Time series are shown for the 3 closest heights of ULID at C1 and SLIDs at E32-E41 as indicated by the legend.

Mean absolute wind speed difference (abs Δ-speed) at all three heights (Fig. 18a), averaged over the period of the observed ramp event at all five sites (09-13 UTC), is also larger at the northern sites (E32, E41) and C1 compared to the southern sites (E37, E39), whereas the average over a longer period (0600-1800 UTC) shows little difference between northern (E32, E41) and southern (E37, E39) sites (Fig. 18b). In comparison, mean Δ-speed for these periods on 20 Aug are significantly smaller (Fig. 18c, d).

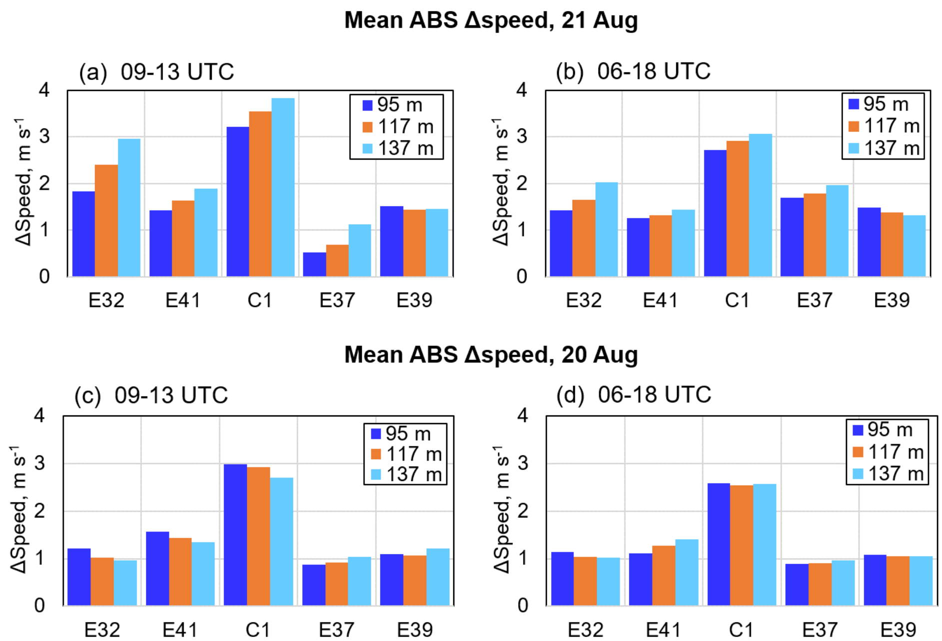

Figure 18. Absolute difference (Δ speed) between HRRRv3 and lidar measurements at five sites averaged over (a) 09-13 UTC and (b) 06-18 UTC on 21 Aug. Forecasts are from the initial time 05z. Same on the bottom panels (c) and (d) but on 20 Aug for 04z forecasts.

8. Conclusions

Changes in the supply of power from wind-generation facilities are a significant issue for the wind energy community. Unpredicted down-ramps are especially problematic, because expected power is suddenly unavailable to the power grid. A significant ramp-down of wind speed, which would have resulted in an abrupt loss of wind power for more than two hours, was observed over north-central Oklahoma during the August 2017 LAFE project. We attributed the ramp to a bore, most likely produced by a gust front from thunderstorm activity to the northwest. It passed over the five-site SGP network of Doppler lidar wind-profiling sensors, allowing the spatial and temporal characteristics of the disturbance to be studied. The high temporal and vertical resolution of Doppler lidar wind profiles made it possible to reliably determine a ramp event observed on 21 Aug 2017 at the ARM SGP sites in central Oklahoma, USA, and analyze the site-to-site variability of the ramp parameters. A significant down-ramp of wind speed passed through the northern and central sites but stalled before reaching the southern sites. The bore caused a significant drop of wind speeds at these sites to below cut-in values of wind turbines in this area.

The ability to accurately predict ramps-down such as found in this study is an important forecasting challenge for wind energy. Predicting the onset of deep moist convection is a difficult problem for current generation NWP forecast models. Even when thunderstorm cells are represented in about the right place in models, the resulting outflows and preceding wave activity, such as the bore in this study, are subject to large errors in timing and other properties of the wind structures, indicating the need for further research into these systems. Supplementary, nested arrays of wind sensors to detect these flows in real time and extrapolate their movement (Banta et al. 2013), or use of wind-turbine mounted anemometers upstream of the disturbances, are other potentially important resources for predicting these ramps an hour to a few hours ahead of time.

Acknowledgments

This study was conducted as part of the Land-Atmosphere Feedback Experiment (LAFE). This research was supported in part by NOAA cooperative agreements NA17OAR4320101 and 375 NA22OAR4320151, the U.S. the U.S. Department of Energy's Atmospheric System Research, an Office of Science Biological and Environmental Research program, under Grant No. DE-SC0020114, as part of the Atmospheric Radiation Measurement Program and Atmospheric System Research Program, and the NOAA Oceanic and Atmospheric Research Office of Weather and Air Quality, the NASA Water and Energy Cycle Program, the German Federal Ministry of Education and Research (BMBF), and the University of Hohenheim. We gratefully acknowledge the efforts of the ARM Southern Great Plains managers and PNLL staff for maintaining and operating that site both during this campaign and over the last three decades. Lastly, the scientific results and conclusions, as well as any views or opinions expressed herein, are those of the authors and do not necessarily reflect the views of NOAA or the Department of Commerce.

Data Availability Statement

Datasets from scanning Doppler lidars at 5 SGP sites used during this study are openly available from the Atmospheric Radiation Measurement (ARM) Southern Great Plains (SGP) Archive at https://www.arm.gov/capabilities/observatories/sgp and in the user manual compiled by T. Shippert, R. Newsom, and L. Riihimaki. ARM Data Center: Atmospheric Radiation

Measurement (ARM) user facility. 2016. Doppler Lidar Horizontal Wind Profiles (DLPROFWIND4NEWS). 2021-06-01 to 2021-08-31, Southern Great Plains (SGP) Waukomis, OK (Extended) (E37). Data set can be accessed at http://dx.doi.org/10.5439/1178582.

The Land Atmosphere Feedback Experiment. Datasets from the Land Atmosphere Feedback Experiment (LAFE, 2017) are available via the ARM Data Discovery portal at: https://adc.arm.gov/discovery/

APPENDICES

Appendix A. Synoptic analysis of BL conditions on 21 Aug

We have characterized the rapid changes of all variables during ~11-14 UTC on 21 August as a bore, generated ahead of a gust front from thunderstorm activity to the northwest of the measurement sites. Here we show supplementary analyses of some meteorological conditions that from the context of this scenario, and some HRRR output for the period of interest.

A.1 Temperature and humidity from North American Regional Reanalysis (NARR)

The North American Regional Reanalysis (NARR) is a model, produced by the National Centers for Environmental Prediction (NCEP), that generates reanalyzed data for temperature, wind, moisture, soil, and dozens of other parameters. The NARR model assimilates a large amount of observational data from a variety of sources to produce a long-term picture of weather over North America. NARR 3-hourly composites of Vector Wind and Precipitable water (Fig. 19a, Appendix A) indicate the southerly flow over the region and a strong peak in water vapor to the north of SGP. Stronger (15-18 m/s) winds over the 09-12 UTC composite (middle panel) diminished by 5-6 m s^{-1} for the 12-15 UTC composites while wind direction changed from southerly to south-westerly. Maps of the Precipitable water (Fig. 19b, Appendix A) show drier conditions in the vicinity during 09-12 UTC. Overall, the ramping event on Aug. 21 occurred during a relatively dry period with the most significant recent rain observed in this area 10 days earlier (Pichugina et al. 2022).

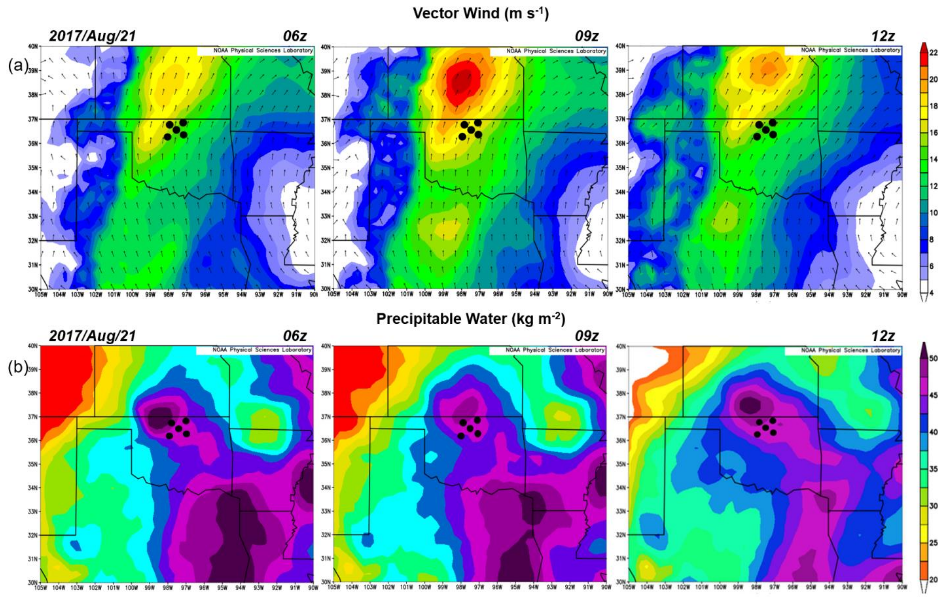

Fig. 19, Appendix A. NARR 3-h composites (averages) of the hourly mean (a) vector wind and (b) precipitable water are shown for periods before (06z), during (09z), and after (12z) the event. The figure was created using *visualization tools at* https://psl.noaa.gov/data/narr/

A.2 Wind speed from the Experimental High Resolution Rapid Refresh (HRRR$_X$) model

HRRRx is the experimental and advanced version of HRRR developed and constantly updated by NOAA/GSL. The version used in this paper is from HRRRv3 (2016-2017), which became operational at the National Weather Service (NWS) on 12 July 2018 with CONUS, Alaska domain coverage. The major changes for HRRRx included improvements in the MYNN PBL scheme (addition of a mass-flux scheme, transition to EDMF framework); and a hybrid vertical coordinate. The major changes for data assimilation: improvements to better retain stratiform clouds; reduced latent heating for radar-identified moist-convective cells introduced into RAP (Dowell et al. 2022; James et al. 2022). HRRRx simulation of 15-min Winds at 80 m and Reflectivity taken for the initial time 3z (Fig. 20a, Appendix A) illustrate the reduction of winds at 1200 UTC compared to winds at 0900 UTC, and the main convective cell moving fairly quickly from the SW to the NE, with substantial activity within an hour or two of the observed ramp timing. The analysis of the NOAA next-generation radar (NEXRAD) images and satellite surface maps (Fig. 20b, Appendix

A) confirms that the convention propagated to the north of the study area. The observed ramp event, larger at the northern sites can be attributed to this convention but the detailed characterization of its propagation is out of the scope of this paper.

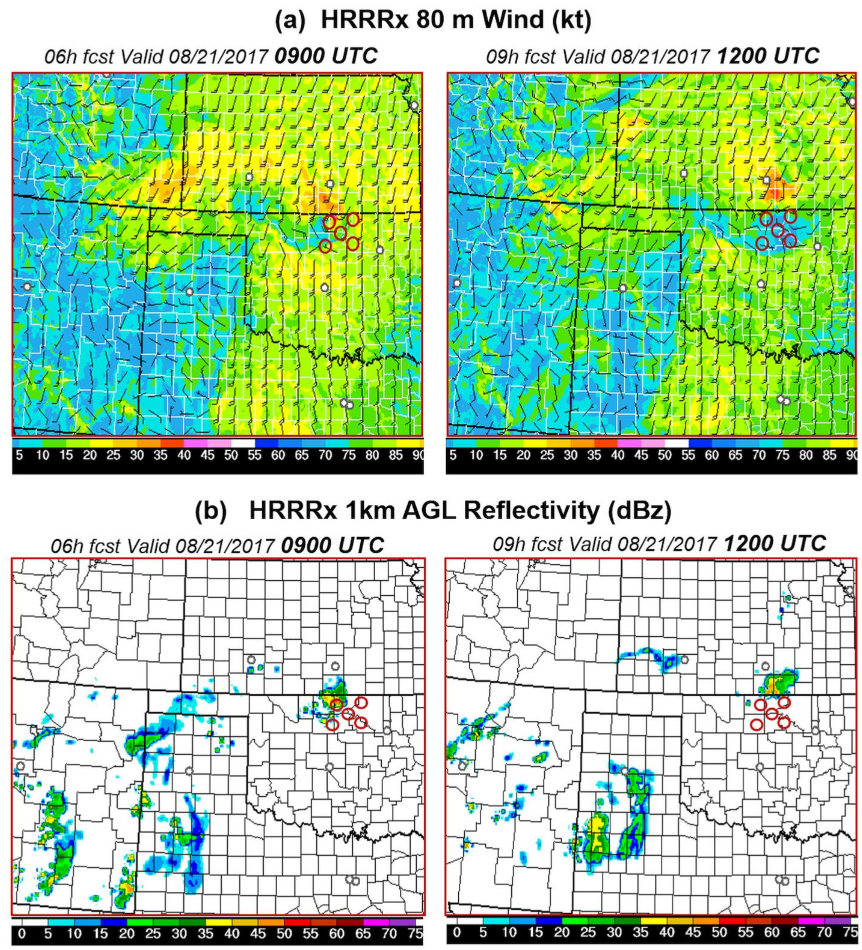

Figure 20, Appendix A. (a) 80-m winds from NOAA/GSL's experimental 3-km HRRRx simulation with 15-min temporal resolution are shown for 0900 UTC (before ramp event) and for 1200 UTC (during ramp event). SGP lidar sites are indicated by the dark red circles. (b) HRRRx 1-km AGL Reflectivity for the same time as in (a).

Accepted to J. Renew. Sustain. Energy 10.1063/5.0161905

Appendix B. The low level jet (LLJ) and basic types of mean wind speed profile observed during previous studies in Great Plains.

The atmospheric flow phenomenon known as the LLJ is a maximum in the boundary layer wind profile (Fig. 21a), frequently observed during warm months throughout the Great Plains of the United States (Bonner 1968; Mitchell et al. 1995; Whiteman et al. 1997; Banta et al. 2003; Song et al. 2005;) Typically LLJ begin to develop around sunset in fair weather conditions, reach peak intensity a few hours after midnight, and dissipate with the onset of daytime convective mixing.

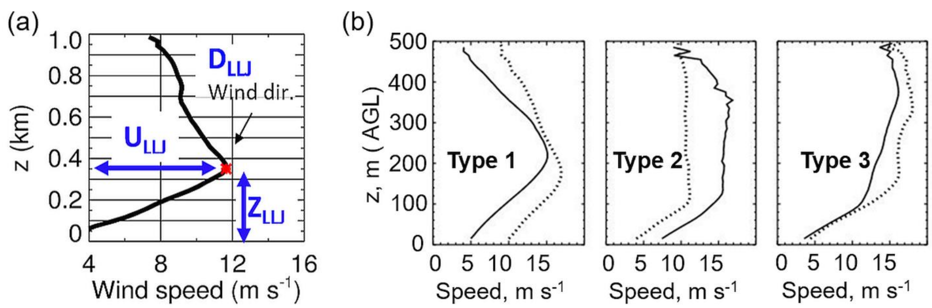

Fig. 21, Appendix B. (a) Definition of the LLJ parameters where the red point indicates the maximum of wind speed (U_{LLJ}) and the height of this maximum (Z_{LLJ}). D_{LLJ} is the corresponding wind direction. (b) Categories of wind profiles that were frequently observed from lidar measurements during the previous experiments in the Great Plains (from Pichugina et al, 2010; ©AMS). Type 1 wind profiles are the classic LLJ shape with a distinct maximum or ‘‘nose”. Type 2 wind profiles represent a uniform or ‘‘flat’’ profile above the shear layer. Type 3 represents wind profiles in which the shear in the subjet layer (and usually the variance profile as well) showed a layered structure.

Data from Doppler sodars, lidars, and other high-resolution observational platforms indicate that peak LLJ winds are often found within 500 m of the ground (Whiteman et al. 1997; Banta et al. 2003; Song et al. 2005). The classic LLJ wind profiles exhibits a distinct maximum or “nose,” with wind speed (**U_{LLJ}**) decreasing both above and below a distinct maximum (Fig. 21a). Increased LLJ winds at night can be an important resource for wind turbine operations in the U.S. Great Plains.

Several mechanisms have been proposed to explain LLJ accelerations in the Great Plains (Blackadar, 1957; Holton, 1967). Here LLJ is taken to mean the vertical layer of the previous

Accepted to J. Renew. Sustain. Energy 10.1063/5.0161905

afternoon's unstable boundary layer that accelerates in response to the nighttime surface cooling (Blackadar,1957). Profiles in this accelerated layer can assume different shapes (Banta et al. 2002, 2006), including the classic LLJ profile, a uniform or "flat" profile, and a layered structure profile as depicted in Fig. 21b. This nocturnal wind acceleration produces a layer of strong shear adjacent to the earth's surface, which generates turbulence. The significant shear-generated turbulence within the layer of wind turbine blades may influence turbine operations.

Appendix C. Composite reflectivity from NEXRAD at 0455 and 0555 UTC.

The smaller disturbance (Fig. 22, Appendix C) was observed just before the major ramp-down event studied in this paper. This lesser disturbance created a significant but shorter-lived ramp event noticed at all sites with the more noticeable at the southwesterly Site E37 around 0500 - 0630 UTC (Fig.14b).

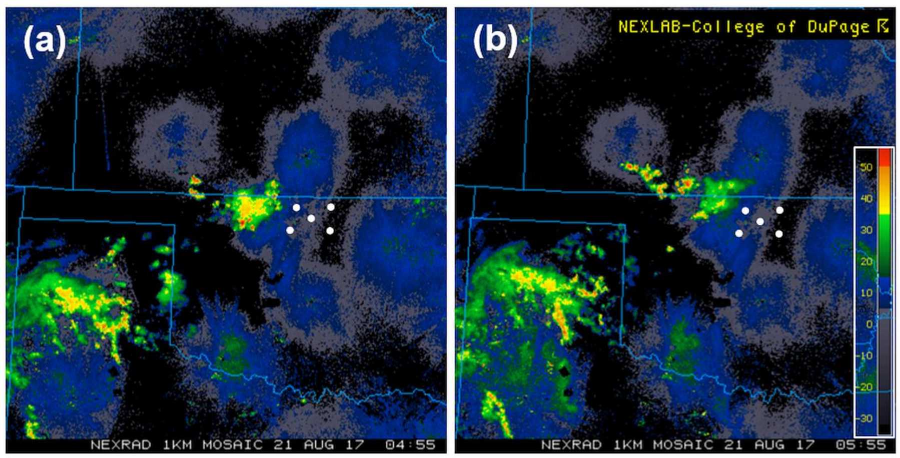

Fig. 22, Appendix C. Composite reflectivity from NEXRAD (Next Generation Radar) 1km MOSAIC on 21 Aug 2017 at (a) 0455 and (b) 0555 UTC. White dots denote approximate locations of SGP measurement sites

Appendix D. Mean wind speed difference between HRRRv3 and lidar measurements

Table 3, Appendix D. Mean over 06-15 UTC wind speed abs difference between HRRRv3, initial times (1z-6z) and lidar data at several heights. Results are shown for smaller ramp days (20, 25, and 30 Aug) in comparison to the significant ramp event observed on 21 Aug.

Date	**Lead time**	**Height, AGL**					
		91 m	***117 m***	***137 m***	***227 m***	***350 m***	***456 m***
20-Aug	**1z**	0.91	0.83	0.80	1.29	1.43	1.62
	2z	1.31	1.27	1.27	1.59	1.32	1.42
	3z	1.32	1.19	1.12	1.36	1.18	1.27
	4z	1.19	1.10	1.07	1.40	1.17	1.27
	5z	-	-	-	-	-	-
	6z	1.70	1.64	1.63	1.92	1.32	1.44
25-Aug	**1z**	-	-	-	-	-	-
	2z	0.60	0.63	0.78	1.08	1.37	1.70
	3z	0.92	1.08	1.22	1.54	1.76	2.18
	4z	0.91	1.06	1.21	1.39	1.46	1.74
	5z	0.94	1.10	1.29	1.62	1.73	2.06
	6z	0.70	0.86	0.93	1.50	1.63	1.70
30-Aug	**1z**	1.55	1.51	1.52	1.08	1.09	1.40
	2z	-	-	-	-	-	-
	3z	1.46	1.30	1.26	0.70	0.72	0.98
	4z	1.72	1.56	1.41	0.84	0.58	0.65
	5z	1.40	1.21	1.09	0.56	0.38	0.63
	6z	1.00	0.84	0.73	0.38	0.59	0.90
21-Aug	**1z**	2.79	2.79	2.76	2.43	1.93	1.88
	2z	2.69	2.37	2.09	2.10	5.40	7.34
	3z	2.20	2.50	2.79	3.94	4.60	5.89
	4z	2.26	2.47	2.65	3.46	4.86	5.73
	5z	3.08	3.17	3.22	2.97	2.78	2.59
	6z	3.19	3.43	3.68	4.03	3.46	2.94

HRRRv3 outputs for some initial times were missing in the NOAA/GSL archive but the corresponding results are clearly show much smaller errors for days with smaller wind ramps. Errors at 91 m, approximately the hub-height of the most turbines in this area, range between 0.60 and 1.72 m s^{-1} on these 3 days in comparison to 2.20-3.19 m s^{-1} on 21 Aug.

Accepted to J. Renew. Sustain. Energy 10.1063/5.0161905

References

Adler, B., Wilczak, J. M., Kenyon, J., Bianco, L., Djalalova, I. V., Olson, J. B., and Turner, D. D.: Evaluation of a cloudy cold-air pool in the Columbia River basin in different versions of the High-Resolution Rapid Refresh (HRRR) model, 2023, *Geosci. Model Dev.*, 16, 597–619, https://doi.org/10.5194/gmd-16-597-2023

Ahn, E.; Hur, J. A Practical Metric to Evaluate the Ramp Events of Wind Generating Resources to Enhance the Security of Smart Energy Systems. *Energie*s 2022, 15, 2676. https://doi.org/10.3390/en15072676

Banta, R.M., Y.L. Pichugina, and R.K. Newsom, 2003: Relationship between low-level jet properties and turbulence kinetic energy in the nocturnal stable boundary layer. J. Atmos. Sci., 60, 2549- 2555.

Banta, R.M., Y.L. Pichugina, N.D. Kelley, W.A. Brewer, and R.M. Hardesty, 2013: Wind-energy meteorology: Insight into wind properties in the turbine rotor layer of the atmosphere from high-resolution Doppler lidar. *Bull. Amer. Meteor. Soc.*, 94, 883-902. DOI:10.1175/BAMS-D-11-00057.1

Banta, R.M., Y.L. Pichugina, W.A. Brewer, A. Choukulkar, K.O. Lantz, J.B. Olson, J. Kenyon, and coauthors, 2020: Characterizing NWP model errors using Doppler-lidar measurements of recurrent regional diurnal flows: Marine-air intrusions into the Columbia-River Basin. *Mon. Wea. Rev*., 148, 929-953; doi.org/10.1175/MWR-D-19-0188.1

Banta, R.M., Y.L. Pichugina, L.S. Darby, W.A. Brewer, J.B. Olson, J.S. Kenyon, and coauthors, 2021: Doppler-lidar evaluation of HRRR-model skill at simulating summertime wind regimes in the Columbia River Basin during WFIP2. *Wea. Forecasting*, 36, 1961-1983. DOI: org/10.1175/WAF-D-21-0012.1

Banta, R.M., Y.L. Pichugina, W.A. Brewer, K.A. Balmes, B. Adler, J. Sedlar, L.S. Darby, D.D. Turner, J.S. Kenyon, E.J. Strobach, B.J. Carroll, J. Sharp, M.T. Stoelinga, J. Cline, and H.J.S. Fernando, 2023: Measurements and model improvement: Insight into NWP model error using Doppler lidar and other WFIP2 measurement systems. *Mon. Wea. Rev*., **152**, (in press), https://doi.org/10.1175/MWR-D-23-0069.1

Benjamin, S.G., S.S. Weygandt, J.M. Brown, M. Hu, C. Alexander, T.G. Smirnova, J.B. Olson, E. James, D.C. Dowell, G.A. Grell, et al. 2016: A North American hourly assimilation and model forecast cycle: The Rapid Refresh. *Mon. Wea. Rev*., 144, 1669-1694;

http://dx.doi.org/10.1175/MWR-D-15-0242.1.

Berg, L. K., L. D. Riihimaki, Y. Qian, H. Yan, and M. Huang, 2015: The Low-Level Jet over the Southern Great Plains Determined from Observations and Reanalyses and Its Impact on Moisture Transport. *J. Climate*, **28**, 6682–6706, https://doi.org/10.1175/JCLI-D-14-00719.1.

Blake, B. T., D. B. Parsons, K. R. Haghi, and S. G. Castleberry, 2017: The structure, evolution, and dynamics of a nocturnal convective system simulated using the WRF-ARW model. *Mon. Wea. Rev*., **145**, 3179–3201, https://doi.org/10.1175/MWR-D-16-0360.1.

Blackadar, A. K. (1957). Boundary layer wind maxima and their significance for the growth of nocturnal inversions. Bulletin of the American Meteorological Society, 38, 283–290. https://doi.org/10.1175/1520-0477-38.5.283

Behrendt, A., V. Wulfmeyer, E. Hammann, S. K. Muppa, and S. Pal, 2015: Profiles of second- to third-order moments of turbulent temperature fluctuations in the convective boundary layer: First measurements with rotational Raman lidar. *Atmos. Chem. Phys.*, 15, 5485–5500, https://doi.org/10.5194/acp-15-5485-2015.

Bianco, L., I.V. Djalalova, J.M. Wilczak, J.B. Olson, et al. 2019: Impact of model improvements on 80 m wind speeds during the second Wind Forecast Improvement Project (WFIP2). *Geosci. Model. Dev.*, 12, 4803-4821; https://doi.org: 10.5194/gmd-12-4803-2019

Bonner, W.D., 1966: Case study of thunderstorm activity in relation to the low-level jet. *Mon. Wea. Rev.*, **94**, 167–178, https://doi.org/10.1175/1520-0493(1966) 094,0167:CSOTAI.2.3.CO;2.

Bonin, T. A., and Coauthors, 2017: Evaluation of turbulence measurement techniques from a single Doppler lidar. *Atmos. Meas. Tech.*, 10, 3021–3039, https://doi.org/10.5194/amt-10-3021-2017.

Bossavy, A.; Girard, R.; Kariniotakis, G. Forecasting Uncertainty Related to Ramps of Wind Power Production. In Proceedings of the EuropeanWind Energy Conference and Exhibition 2010, *EWEC* 2010, Warsaw, Poland, 20 April 2010.

Brian J. Carroll, Brian J., Belay B. Demoz, Ruben Delgado, 2019: An Overview of Low-Level Jet Winds and Corresponding Mixed Layer Depths During PECAN. J. Geophysical Research: Atmospheres, 124,9141-9160, DOI: 10.1029/2019JD030658

Dalton, A., Bekker, B., & Koivisto, M. J., 2021: Simulation and detection of wind power ramps and identification of their causative atmospheric circulation patterns. Electric Power Systems Research, 192, [106936].https://doi.org/10.1016/j.epsr.2020.106936

Davies, L., Reeder, M. J., & Lane, T. P. (2017). A climatology of atmospheric pressure jumps over southeastern Australia. *Quarterly Journal of the Royal Meteorological Society*, *143*(702), 439–449. https://doi.org/10.1002/qj.2933

DeMarco, A, Basu, S. On the tails of the wind ramp distributions. *Wind Energy*. 2018; 21: 892–905. https://doi.org/10.1002/we.2202

Deppe, A. J., Gallus, W. A., and Takle, E. S.: A WRF Ensemble for Improved Wind Speed Forecasts at Turbine Height, 2012, *Weather and Forecasting*, 28, 212–228, https://doi.org/10.1175/WAF-D-11-00112.1

Dowell D.C., Curtis A. R., James E. P. , et al. 2022; The High-Resolution Rapid Refresh (HRRR): An Hourly Updating Convection-Allowing Forecast Model. Part I: Motivation and System Description, *Weather and Forecasting*, 37(8), DOI: 10.1175/WAF-D-21-0151.1

Drew D. R, Janet F. Barlow, Phil J. Coker, 2018: Identifying and characterising large ramps in power output of offshore wind farms, Renewable Energy, 127, pp 195-203, https://doi.org/10.1016/j.renene.2018.04.064.

Draxl, C., R. Worsnop, G. Xia, D. Chand, J. K. Lundquist, Y. Pichugina, J. Sharp, G. Wedam, J. Wilczak, and L. Berg, 2021: Mountain waves impact wind power generation, *Wind Energy Science*., 6 (1), DOI:10.5194/wes-6-45-2021

Ela E. and Kemper J., 2009: Wind Plant Ramping Behavior. *Technical Report NREL/TP-550-46938*

Ferreira, C., Gama, J., Matias, L., Botterud, A., Wang, J., and INESC Porto. A survey on wind power ramp forecasting. United States: N. p., 2011: doi:10.2172/1008309.

Freedman, J., M Markus, R. Penc- AWS Truewind, LLC, 2008: Analysis of West Texas wind plant ramp-up and ramp-down events. Available online at: http://interchange.puc.state.tx.us/WebApp/Interchange/Documents/33672_1014_580034.

Freedman J. and Zack J., Identifying Ramp Events, 2012: May 12, 2012, • *National Wind Watch*.

Fritsch J. M., R. J. Kane and C. R. Chelius, 1986: The Contribution of Mesoscale Convective Weather Systems to the Warm-Season Precipitation in the United States, J. *Climate and Applied Meteorology,* **25**, 1333-1345, https://www.jstor.org/stable/26182571

Haghi, K. R., D.B. Parsons, and A. Shapiro, 2017: Bores observed during IHOP_2002: The relationship of bores to the nocturnal environment. *Mon. Wea. Rev.*, **145**, 3929–3946, https://doi.org/10.1175/MWR-D-16-0415.1.

Haghi, K.R., B. Geerts, H.G. Chipilski, A. Johnson, S. Degelia, D. Imy, D.B. Parsons, R.D. Adams-Selin, D.D. Turner, and X. Wang, 2019: Bore-ing into nocturnal convection. *Bull. Amer. Meteor. Soc.*, **100**, 1103-1121, https://doi.org/10.1175/BAMS-D-17-0250.1

James, E. P., Alexander, C. R., Dowell, D. C., Weygandt, S. S., Benjamin, S. G., Manikin, G. S., Brown, J. M., Olson, J. B., Hu, M., Smirnova, T. G., Ladwig, T., Kenyon, J. S., & Turner, D. D. (2022). The High-Resolution Rapid Refresh (HRRR): An Hourly Updating Convection-Allowing Forecast Model. Part II: Forecast Performance, *Weather and Forecasting*, *37*(8), 1397-1417. DOI: https://doi.org/10.1175/WAF-D-21-0130.1

Johnson, A., X. Wang, K. Haghi, and D. Parsons, 2018: Evaluation of forecasts of a convectively generated bore using an intensively observed case study from PECAN. *Mon. Wea. Rev.*, **146**, 3097–3122, https://doi.org/10.1175/MWR-D-18-0059.1.

Gallego, Cristóbal & Cuerva, Alvaro & Costa, Alexandre, 2014: Detecting and characterizing ramp events in wind power time series. Journal of Physics: Conference Series. 555. 012040. 10.1088/1742-6596/555/1/012040.

GE Energy: 1.5MW wind turbine, 2009. Available online at https://en.wind-turbine-models.com/turbines/655-ge-general-electric-ge-1.5sle

Greaves, B.; Collins, J.; Parkes, J.; Tindal, A. Temporal Forecast Uncertainty for Ramp Events. Wind Eng. 2009, 33

Geerts, B., and Coauthors, 2017: The 2015 Plains Elevated Convection at Night Field Project. *Bull. Amer. Meteor. Soc.*, **98**, 767–786, https://doi.org/10.1175/BAMS-D-15-00257.1.

Hammann, E., A. Behrendt, F. Le Mounier, and V. Wulfmeyer, 2015: Temperature profiling of the atmospheric boundary layer with rotational Raman lidar during the HD(CP)2 Observational Prototype Experiment. *Atmos. Chem. Phys.*, 15, 2867–2881, https://doi.org/10.5194/acp-15-2867-2015.

Knupp, K., 2006: Observational analysis of a gust front to bore to solitary wave transition within an evolving nocturnal boundary layer. *J. Atmos. Sci.*, 63, 2016–2035, doi:10.1175/JAS3731.1.

Koch, S.E., S.H. Melfi, W.C. Skillman, D. Whiteman, P.B. Dorian, and R. Ferrare, 1991: Structure of an internal bore and dissipating gravity current as revealed by Raman lidar. *Mon. Wea. Rev*., 119, 857–887, doi:10.1175/1520-0493(1991)119,0857:SOAIBA.2.0.CO;2.

Koch, S.E., W. Feltz, F. Fabry, M. Pagowski, B. Geerts, K. M. Bedka, D. O. Miller, and J. W. Wilson, 2008a: Turbulent mixing processes in atmospheric bores and solitary waves deduced from profiling systems and numerical simulation. *Mon. Wea. Rev*., 136, 1373–1400, doi:10.1175/2007MWR2252.1.

Koch, S.E., C. Flamant, J. W. Wilson, B. M. Gentry, and B. D. Jamison, 2008b: An atmospheric soliton observed with Doppler radar, differential absorption lidar, and a molecular Doppler lidar. *J. Atmos. Oceanic Technol*., 25, 1267–1287, doi:10.1175/2007JTECHA951.1.

Lee, D.; Kim, J.; Baldick, R. Ramp Rates Control of Wind Power Output Using a Storage System and Gaussian Processes; University of Texas at Austin, Electrical and Computer Engineering: Austin, TX, USA, 2012.)

Lee, T. R., and M. Buban, 2020: Evaluation of Monin-Obukhov and bulk Richardson parameterizations for surface-atmosphere exchange. Journal of Applied Meteorology and Climatology, 59 (6), 1091-1107, https://doi.org/10.1175/JAMC-D-19-0057.1.

Lee, T. R., M. S. Buban, and T. P. Meyers, 2021: Application of bulk Richardson parameterizations of surface fluxes to heterogeneous land surfaces. Monthly Weather Review, 149, 3243-3264, https://doi.org/10.1175/MWR-D-21-0047.1

Loveless, D M., T J. Wagner, D.D. Turner, S.A. Ackerman, and W.F. Feltz, 2019: A composite perspective on bore passages during the PECAN campaign. Mon. Wea. Rev., 147, 1395–1413, https://doi.org/10.1175/MWR-D-18-0291.1.

Martin, E. R., & Johnson, R. H. (2008). An observational and modeling study of an atmospheric internal bore during NAME 2004. *Monthly Weather Review*, *136*(11), 4150–4167. https://doi.org/10.1175/2008MWR2486.1

McCaffrey, K., J.M. Wilczak, L. Bianco, E. Grimit, J. Sharp, R.M. Banta, K. Friedrich, H.J.S. Fernando, R. Krishnamurthy, L.S. Leo and P. Muradyan, 2019: Identification and characterization of persistent cold pool events from temperature and wind profilers in the Columbia River Basin. *J. Appl. Meteor. Climatol.*, 58, 2533-2551, https://doi.org/10.1175/JAMC-D-19-0046.1.

Mitchell, M.J., R.W. Arritt, and K. Labas, 1995: A climatology of warm season Great Plains low-level jet using wind profiler observations. *Wea. Forecasting*, **10**, 576–591, DOI:10.1175/1520-0434(1995)010<0576:ACOTWS>2.0.CO;2

Mueller, D., B. Geerts, Z. Wang, M. Deng, and C. Grasmick, 2017: Evolution and vertical structure of an undular bore observed on 20 June 2015 during PECAN. *Mon. Wea. Rev*., 145, 3775–3794, doi:10.1175/MWR-D-16-0305.1.

Newsom, R.K. and Krishnamurthy R, 2020: Doppler Lidar (DL) Instrument Handbook, DOE/SC ARM-TR-101.

Olson, J.B., J.S. Kenyon, I. Djalalova, L. Bianco, D.D. Turner, Y. Pichugina, A. Choukulkar, M.D. Toy, J.M. Brown, W.M. Angevine, E. Akish, J.-W. Bao, P. Jimenez, B. Kosovic, K.A. Lundquist, C. Draxl, J.K. Lundquist, J. McCaa, K. McCaffrey, K. Lantz, C. Long, J. Wilczak, R. Banta, M. Marquis, S. Redfern, L.K. Berg, W. Shaw, and J. Cline, 2019: Improving wind energy forecasting through numerical weather prediction model development. *Bull. Amer. Meteor. Soc.*, 100, 2201-2220; doi.org/10.1175/BAMS-D-18-0040.1

Osborne, S. R., and A. Lapworth, 2017: Initiation and Propagation of an Atmospheric Bore in a Numerical Forecast Model: A Comparison with Observations. *J. Appl. Meteor. Climatol.*, **56**, 2999–3016, https://doi.org/10.1175/JAMC-D-17-0045.1.

Parker, M.D., 2021: Self-Organization and Maintenance of Simulated Nocturnal Convective Systems from PECAN. *Mon. Wea. Rev*., **149**, 999-1022. https://doi.org/10.1175/MWR-D-20-0263.1

Parsons, D.B., K.R. Haghi, K.T. Halbert, B. Elmer, and J. Wang, 2019: The potential role of atmospheric bores and gravity waves in the initiation and maintenance of nocturnal convection over the Southern Great Plains. *J. Atmos. Sci.*, **76**, 43–68, https://doi.org/10.1175/JAS-D-17-0172.1.

Pichault, M., C. Vincent, G. Skidmore, and J. Monty (2021). Characterization of intra-hourly wind power ramps at the wind farm scale and associated processes, Wind Energy Science, 6 (1), 131--147, DOI:10.5194/wes-6-131-2021

Pichugina, Y. L., Banta R. M., 2010: Stable boundary-layer depth from high-resolution measurements of the mean wind profile. J. Appl. Meteor. Climatol. 2010; 49: 20–35, https://doi.org/10.1175/2009JAMC2168.1.

Pichugina, Y. L., R.M. Banta, J.B. Olson, J.R. Carley, M.C. Marquis, W.A. Brewer, J.M. Wilczak, I. V. Djalalova, L. Bianco, E.P. James, S.G. Benjamin, and J. Cline, 2017: Assessment of NWP forecast models in simulating offshore winds through the lower boundary layer by measurements from a ship-based scanning Doppler lidar. Monthly *Weather Review*, vol. 145, no. 10, 4277-4301 doi: 10.1175/MWR-D-16-0442.1

Pichugina, Y.L., R.M. Banta, and Coauthors, 2019: Spatial variability of winds and HRRR-NCEP model error statistics at three Doppler-lidar sites in the wind-energy generation region of the Columbia River Basin. *J. Appl. Meteor. Climatol.*, 58, 1633-1656. doi.org/10.1175/JAMC-D-11-040.1

Pichugina, Y. L., W.A. Brewer, R.M. Banta, L. Bianco, C. Draxl, J. Kenyon, J. K. Lundquist, J.B. Olson, D.D. Turner, S. Wharton J. Wilczak, S. Baidar, L.K. Berg, H.J.S. Fernando, B.J. McCarty, R. Rai, B. Roberts, J. Sharp, W.J. Shaw, M.T. Stoelinga, and R. Worsnop, 2020. Evaluating the WFIP2 updates to the HRRR model using scanning Doppler lidar measurements in the complex terrain of the Columbia River Basin, *J. Renewable and Sustainable Energy (JRSE)*, 12(4):27 pp. (2020). https://doi.org/10.1063/5.0009138

Pichugina, Y. L., Banta, R. M., Brewer, W. A., Kenyon, J., Olson, J. B., Turner, D. D., Wilczak, J., Baidar, S., Lundquist, J. K., Shaw, W. J., & Wharton, S. (2022). Model Evaluation by Measurements from Collocated Remote Sensors in Complex Terrain, *Weather and Forecasting*, *37*(10), 1829-1853. https://doi.org/10.1175/WAF-D-21-0214.1

Pichugina Y. L., R. M. Banta, W. Alan Brewer, D.D. Turner, V.O. Wulfmeyer, E.J. Strobach, S. Baidar, and B.J. Carroll (2023): Doppler lidar measurements of wind variability and LLJ properties in Central Oklahoma during the August 2017 Land-Atmosphere Feedback Experiment. *J. Appl. Meteor. Climatol*, **62**, 947-969, DOI: 10.1175/JAMC-D-22-0128.1, 2023

Rai, R., L. Berg, R. Newsom, C. Kaul, J. Mirocha, A. Choukulkar, A. Brewer, Y. Pichugina, and R. Banta, 2020: Characterization of turbulence under different stability conditions using lidar scanning data, *Journal of Physics*, 1452, doi:10.1088/1742-6596/1452/1/012085

Rottman, J. W., and J. E. Simpson, 1989: The formation of internal bores in the atmosphere: A laboratory model. *Quart. J. Roy. Meteor. Soc*., 115, 941–963, doi:10.1002/qj.49711548809.

Shaw, W.J., L.K Berg, J. Cline, C. Draxl, E. Grimit, J.K. Lundquist, M. Marquis, J. McCaa, J. Olson, C. Sivaraman, J. Sharp, J. Wilczak, 2019: The Second Wind Forecast Improvement

Project (WFIP 2): General overview. *Bull. Amer. Meteor. Soc.*, 100, 1687-1699; doi.org/10.1175/BAMS-D-18-0036.1

Sherry, M. and 470 Rival, D., 2015: Meteorological Phenomena Associated with Wind-Power Ramps Downwind of Mountainous Terrain, *Journal of Renewable and Sustainable Energy*, 7, 033 101, https://doi.org/10.1063/1.4919021

Smith, N. H., & Ancell, B. C., 2017:. Ensemble Sensitivity Analysis of Wind Ramp Events with Applications to Observation Targeting, *Monthly Weather Review*, *145*(7), 2505-2522. https://doi.org/10.1175/MWR-D-16-0306.1

Song, J., K. Liao, R.L. Coulter, and B.M. Lesht, 2005: Climatology of the low-level jet at the Southern Great Plains Atmospheric Boundary Layer Experiments site. *J. Appl. Meteor.*, 44, 1593–1606, https://doi.org/10.1175/JAM2294.1.

Stelten, S., and W.A. Gallus Jr., 2017: Pristine nocturnal convective initiation: A climatology and preliminary examination of predictability. *Wea. Forecasting*, **32**, 1613–1635, https://doi.org/10.1175/WAF-D-16-0222.1.

Toms, B.A., J.A. Tomaszewski, D.D. Turner, and S.E. Koch, 2017: Analysis of a lower-tropospheric gravity wave train using direct and remote sensing measurement systems. *Mon. Wea. Rev*., 145, 2791–2812, doi:10.1175/MWR-D-16-0216.1.

Tripoli G. and W.R. Cotton, 1989: A numerical Study an observed orogenic mesoscale convective system. Part 2: Analysis of governing dynamics. *Mon. Wea. Rev*., **117**, 301-324.

Turner D.D and U. Loehnert, Information Content and Uncertainties in Thermodynamic Profiles and Liquid Cloud Properties Retrieved from the Ground-Based Atmospheric Emitted Radiance Interferometer (AERI), J Appl Met Clim, vol 53, pp 752-771, 2014, doi:10.1175/JAMC-D-13-0126.1

Wallace, J. M., 1975: Diurnal Variations in Precipitation and Thunderstorm Frequency over the Conterminous United States. *Mon. Wea. Rev.*, **103**, 406–419, https://doi.org/10.1175/1520-0493(1975)103<0406:DVIPAT>2.0.CO;2.

Wharton, S; Lundquist, J K; Marjanovic, N; Williams, J L; Rhodes, M; Chow, T K et al., 2011: Review of Wind Energy Forecasting Methods for Modeling Ramping Events, report, March 28, 2011; Livermore, California. https://digital.library.unt.edu

Whiteman, C.D., X. Bian, and S. Zhong, 1997: Low-level jet climatology from enhanced rawinsonde observations at a site in the Southern Great Plains. *J. Appl. Meteor.*, **36**, 1363–1375, https://doi.org/10.1175/1520-0450(1997)036,1363:LLJCFE.2.0.CO;2.

Wilczak, J.M., M. Stoelinga, L.K. Berg, J. Sharp, C. Draxl, K McCaffrey, R.M. Banta, L. Bianco, I. Djalalova, J.K. Lundquist, P. Muradyan, A. Choukulkar, L. Leo, T. Bonin, Y. Pichugina, R. Eckman, C.N. Long, K. Lantz, R.P. Worsnop, J. Bickford, N. Bodini, D. Chand, A. Clifton, J. Cline, D.R. Cook, H.J.S. Fernando, K. Friedrich, R. Krishnamurthy, M. Marquis, J. McCaa, J.B. Olson, S. Otarola-Bustos, G. Scott, W.J. Shaw, S. Wharton, A.B. White, 2019: The Second Wind Forecast Improvement Project (WFIP2): Observational field campaign. *Bull. Amer. Meteor. Soc*., 100, 1701-1723; doi.org/10.1175/BAMS-D-18-0035.1

Worsnop, R. P., Scheuerer, M., Hamill, T. M., and Lundquist, J. K.: Generating wind power scenarios for probabilistic ramp event prediction using multivariate statistical post-processing, 2018: *Wind Energ. Sci*., 3, 371–393, https://doi.org/10.5194/wes-3-371-2018

Wulfmeyer, V., D.D. Turner, B. Baker, R. Banta, A. Behrendt, T. Bonin, W.A. Brewer, M. Buban, A. Choukulkar, E Dumas, RM Hardesty, T Heus, J Ingwersen, D Lange, TR Lee, S Metzendorf, SK Muppa, T. Meyers, R Newsom, M Osman, S Raasch, J Santanello, C Senff, F Späth, T Wagner, T Weckwerth, 2018: "A new research approach for observing and characterizing land-atmosphere feedback." *Bull. Amer. Meteor. Soc.*, 99(8), 1639-1667, http://dx.doi.org/10.1175/BAMS-D-17-0009.1.

Yang, Qing & Berg, Larry & Pekour, Mikhail & Fast, Jerome & Newsom, Rob & Stoelinga, Mark & Finley, Catherine, 2013: Evaluation of WRF-Predicted Near-Hub-Height Winds and Ramp Events over a Pacific Northwest Site with Complex Terrain. *Journal of Applied Meteorology and Climatolog*y. 52. 1753-1763. 10.1175/JAMC-D-12-0267.1.

Zhang, J, Florita, A, Hodge, B, & Freedman, J., 2014: Ramp Forecasting Performance From Improved Short-Term Wind Power Forecasting, *Proceedings of the ASME 2014 International Design Engineering Technical Conferences and Computers and Information in Engineering Conference*. *Volume 2A: 40th Design Automation Conference*. Buffalo, New York, USA. 2014. V02AT03A022. ASME. https://doi.org/10.1115/DETC2014-34775

Zhang, S., Parsons, D. B., Xu, X., Sun, J., Wu, T., Xu, F., et al. (2022). Bores observed during the warm season of 2015–2019 over the southern North China Plain. *Geophysical Research Letters*, *49*, e2022GL099205. https://doi. org/10.1029/2022GL099205